



X-chromosome influences on neuroanatomical variation in humans

Travis T. Mallard^{1,2}, Siyuan Liu^{1,2}, Jakob Seidlitz^{1,2}, Zhiwei Ma^{1,2}, Dustin Moraczewski⁴, Adam Thomas^{1,2} and Armin Raznahan^{1,2}✉

The X-chromosome has long been hypothesized to have a disproportionate influence on the brain based on its enrichment for genes that are expressed in the brain and associated with intellectual disability. Here, we verify this hypothesis through partitioned heritability analysis of X-chromosome influences (XIs) on human brain anatomy in 32,256 individuals from the UK Biobank. We first establish evidence for dosage compensation in XIs on brain anatomy—reflecting larger XIs in males compared to females, which correlate with regional sex-biases in neuroanatomical variance. XIs are significantly larger than would be predicted from X-chromosome size for the relative surface area of cortical systems supporting attention, decision-making and motor control. Follow-up association analyses implicate X-linked genes with pleiotropic effects on cognition. Our study reveals a privileged role for the X-chromosome in human neurodevelopment and urges greater inclusion of this chromosome in future genome-wide association studies.

Our understanding of genetic contributions to human brain development has dramatically expanded over the past 5 years through access to large study populations that combine both genotypic and neuroimaging data. In particular, pioneering imaging–genetics studies from the ENIGMA consortium and the UK Biobank (UKB) dataset have started to reveal the relationship between neuroanatomical variation in health and genotypic variation tagged by common single nucleotide polymorphisms (SNPs)^{1–3}. This work has revealed the pervasive and diverse influence of genes on brain morphology, reflected by moderate-to-high heritability estimates and complex genetic architectures across anatomical subdivisions of the human brain. However, to date, most large-scale studies linking ‘genome-wide’ SNP data to neuroimaging phenotypes have excluded the sex chromosomes (with few exceptions⁴), presumably because they require a unique analytic approach⁵. Notably, analysis of sex chromosomes must grapple with the following facts: (1) X- and Y-chromosome dosage differs between males (XY) and females (XX), and (2) one X-chromosome is randomly silenced in all cells of females through the process of X-inactivation⁶.

The current lack of data regarding sex chromosome influences on human brain organization in health is especially problematic when one considers several lines of evidence indicating that the X-chromosome might in fact have a disproportionately strong influence on brain development relative to other chromosomes. Specifically, it is known that X-chromosome genes show enriched expression in brain tissue relative to other chromosomes⁷, and the X-chromosome is enriched for genes that cause intellectual disability when mutated⁸. Furthermore, X-chromosome aneuploidy induces robust regional changes in human brain anatomy as measured by structural MRI⁹. These observations naturally lead to the as yet untested prediction that common genetic variation on the X-chromosome exerts an ‘oversized’ influence on human brain development as captured by measures of regional brain anatomy from structural MRI. In the present study, we directly test this

prediction by leveraging well-substantiated theory from statistical genetics and large-scale data from the UKB ($n=32,256$ individuals of European ancestry, 52.97% female, mean age = 64.31 years) to provide the first map of enriched X-chromosome influences (enriched XIs) on normative neuroanatomical variation in humans. To this aim, we performed a series of genome-based restricted maximum likelihood (GREML)^{10,11} analyses to facilitate the following investigations: (1) evaluate evidence for X-chromosome dosage compensation in males and females; (2) partition total SNP-based heritability (h_g^2) across the autosomes (h_a^2) and the X-chromosome (h_X^2); and (3) test for enriched XIs on both global and regional measures of brain anatomy. We annotate observed XIs using spatial comparison with neuroimaging-derived maps of brain structure and function and with follow-up brain-region-specific X-chromosome-wide association (XWA) analyses.

All global and regional measures of brain anatomy were estimated using the FreeSurfer pipeline^{12,13} (Methods). We examined diverse regional measures, including subcortical volumes and cortical volumes (CVs), as well as regional cortical surface area (SA) and cortical thickness (CT). Cortical phenotypes were estimated for each of the 358 regions of interest (ROIs) as defined by a recent multimodal parcellation from the Human Connectome Project (HCP-parcellation)¹⁴. Separate analysis of SA, CT and CV was motivated by the following considerations: SA and CT together determine CV, but differ greatly in their genetic, developmental and cellular determinants¹⁵; variation in SA is known to explain the bulk of CV variation across individuals and shows higher genetic correlation with CV variation than CT¹⁶; and SA and CT differ in their genetic architecture such that SA is a less polygenic trait than CT, and is associated with larger absolute variant-specific effect sizes¹⁷. Given these considerations, and the observed distribution of XIs in our analyses (see below), we focus our manuscript on findings for regional SA and provide equivalent results for all other anatomical phenotypes in the supplementary materials.

¹Department of Psychology, University of Texas at Austin, Austin, TX, USA. ²Section on Developmental Neurogenomics, Human Genetics Branch, National Institute of Mental Health Intramural Research Program, Bethesda, MD, USA. ³Laboratory of Functional and Molecular Imaging, National Institute of Neurological Disorders and Stroke, National Institutes of Health, Bethesda, MD, USA. ⁴Data Science and Sharing Team, National Institute of Mental Health, Bethesda, MD, USA. ✉e-mail: raznahana@mail.nih.gov

Results

X-chromosome dosage compensation and sex-biased XIs. To appropriately estimate h_g^2 while incorporating the X-chromosome, it is necessary to first determine whether h_X^2 should be modeled assuming full dosage compensation (under which X-linked genetic variance is greater in males than females), no dosage compensation (which would predict the opposite sex-bias in X-linked variance) or equal variance across men and women¹¹. By comparing the fit of these models, we found evidence of full dosage compensation for all global measures of brain anatomy, as well as the vast majority of regional measures (Supplementary Tables 1–5). This finding implies that the X-chromosome tends to explain a greater proportion of neuroanatomical variation in males than females. To provide a complementary test of this inference, we used sex-stratified analyses to separately estimate h_X^2 in males and females for the 920 cortical and subcortical ROIs for which the full dosage compensation model fit best. Across these phenotypes, the median h_X^2 in males was 2.37-times larger (bootstrapped 95% confidence interval (CI)=1.70–3.25) than the median h_X^2 in females (Wilcoxon $P=1.18 \times 10^{-23}$; Extended Data Fig. 1 and Methods).

Although we observed robust statistical support for full dosage compensation for almost all measures of regional brain anatomy (Fig. 1a (SA), Extended Data Figs. 2a (CV) and 3a (CT), and Supplementary Tables 1–5), there was substantial variation in the magnitude of this effect across the cortical sheet (Fig. 1b (SA), Extended Data Figs. 2b (CV) and 3b (CT), and Supplementary Tables 2–4). We reasoned that the sex biases in XI arising from full dosage compensation could potentially contribute to known sex biases in regional anatomical variance, which are particularly pronounced for cortical SA^{18,19}. To test this hypothesis, we computed the male:female ratio of SA variance for each cortical ROI in the UKB sample (Fig. 1c and Methods) and correlated inter-ROI differences in this metric, with inter-ROI differences in the strength of statistical support for full dosage compensation (Fig. 1d). We observed a strong positive correlation between these two features of the cortical sheet ($r=0.76$; Fig. 1d), which is consistent with a model in which regional sex-biases in XIs on SA variance contribute to regional sex-biases in SA variance.

XIs on neuroanatomical variation. Having determined the suitable X-chromosome dosage compensation model for each anatomical measure of interest (Supplementary Tables 1–5), we next used GREML^{10,11} to estimate h_g^2 , which we further partitioned into h_a^2 and h_X^2 . This partitioning enabled us to test whether observed XIs on neuroanatomical variation were in excess of those predicted by the size of the X-chromosome genomic partition (corresponding to the theoretical null of equal per-SNP heritability). Drawing on existing methods for partitioning heritability^{10,11,20}, we calculated the ratio of the proportion of heritability explained by the X-chromosome to the proportion of genomic base pairs located on the X-chromosome (~5%; Methods). This provided an intuitive index of the magnitude of XI enrichment (ratios > 1) or depletion (ratios < 1) for each phenotype. Furthermore, to test whether the observed enrichment or depletion of XI was statistically significant, we used a monotonically related enrichment Z-test to obtain a corresponding P value (Methods).

We first considered global measures of brain anatomy, including total brain volume and surface-based estimates of total SA and mean CT. Our estimate of SNP-based h_a^2 for total brain volume was in line with that reported by a prior study³ using GREML in both releases of the UKB (72% versus 71%; Supplementary Table 1 and Methods). We observed a significant depletion of XIs for total brain volume ($P=3 \times 10^{-4}$), with the observed h_X^2 reaching only 60% of the expected h_X^2 based on the size of the X-chromosome compartment (2.3% observed versus 3.8% expected; $h_g^2=74\%$). Our estimates of h_a^2 for total cortical SA and mean CT (77% and 57%,

respectively) were substantially larger than those reported by prior studies^{1,21} using summary statistics from genome-wide association studies (GWAS; excluding the X-chromosome) in a multisample cohort¹ (34% and 26%, respectively) and both releases of the UKB data²¹ (32% and 23%, respectively). Of note, our observation that h_a^2 estimates from GREML are larger than those produced by methods based on GWAS summary statistics is in line with published methodological comparisons of these methods in both simulated²² and real²³ data. We also observed a significant depletion of XIs for total SA and mean CT ($P<9 \times 10^{-4}$, XIs ~50% of expectation from X-chromosome size, $h_g^2=79\%$ and 59%, respectively). The depletion of XIs for measures of global brain anatomy implies that any enriched XIs on human neuroanatomical variation would need to operate at a more local scale involving the relative size of subcomponents of the brain. To test this idea, we conducted GREML analyses of regional anatomical traits after regressing out the appropriate global trait (for example, regional volume controlling for total brain volume, regional CT controlling for overall mean CT and regional SA controlling for total SA).

Our GREML-based estimates of h_g^2 for measures of regional brain anatomy in the full UKB sample (Supplementary Tables 2–5 and Methods) reinforced prior reports¹ of higher heritability for regional SA compared to regional CT (Supplementary Tables 2 and 3), and substantial inter-regional variation in heritability across the cortical sheet (Fig. 2a (SA) and Extended Data Figs. 4a (CV) and 5a (CT)). Importantly, our estimates of h_a^2 were closely aligned with those reported in a prior study³ that also used a GREML approach to estimate heritability in an earlier release of the UKB imaging data. Specifically, the ranges of h_a^2 for comparable subcortical volumetric phenotypes examined in both studies were very similar, being 31–63% in our study (mean 48%) and 33–63% (mean 54%) in the study by Zhao and colleagues³. We used autosome-only GREML analyses to test and verify the expectation that estimates of total heritability would be consistently greater with inclusion compared to exclusion of the X-chromosome (Supplementary Tables 2–5). The mean proportion of h_g^2 lost by exclusion of the X-chromosome was greatest for regional measures of SA (mean cross-ROI heritability loss for SA = 7.58% (95% CI = 7.14–8.02%)), lowest for CT (2.83% (95% CI = 2.47–3.19%)) and intermediate for their product, CV (6.59% (95% CI = 6.23–6.94%)). The proportion of SA heritability lost from exclusion of the X-chromosome was remarkably large for several ROIs (Supplementary Table 2). For example, although the X-chromosome accounts for ~5% of the genome, the proportion of h_g^2 explained by the X-chromosome partition exceeded 20% for relative SA of several cortical regions, including the right superior parietal cortex (areas 7pl and LIPv in ref. ¹⁴), the right premotor cortex (area PEF¹⁴), the right entorhinal cortex (area ec¹⁴), the left ventral postcentral cortex (area 43¹⁴), the left perisylvian cortex (area PSL¹⁴) and the left supramarginal cortex (area p_fm¹⁴).

The magnitude of XIs (that is, h_X^2) varied substantially across brain regions and phenotypes (Fig. 2b (SA), Extended Data Figs. 4b (CV) and 5b (CT), and Supplementary Tables 2–5), as did the ratio between observed and expected XIs on human brain anatomy (XI ratio) (Fig. 2c (SA), Extended Data Figs. 4c (CV) and 5c (CT), and Supplementary Tables 2–5). We did not find evidence for enriched XIs on any regional measure of subcortical volume (Supplementary Table 5). In the cortex, observed XI ratios were consistently greater for regional measures of SA and CV than CT (Extended Data Fig. 6a). For example, ~66% of SA ROIs showed an XI ratio greater than 1, whereas only ~18% of ROIs met this criterion for CT (Supplementary Tables 2 and 3). We also observed a strikingly stronger spatial coupling between regional variation in the XI ratio for SA and CV than for CT and CV ($r=0.72$ and $r=0.11$, respectively; Extended Data Fig. 6b,c). There was a weak spatial coupling between the XI ratio for SA and CT ($r=0.15$; Extended Data Fig. 6d). Taken together, these results indicate that enriched XIs on cortical anatomy are much more

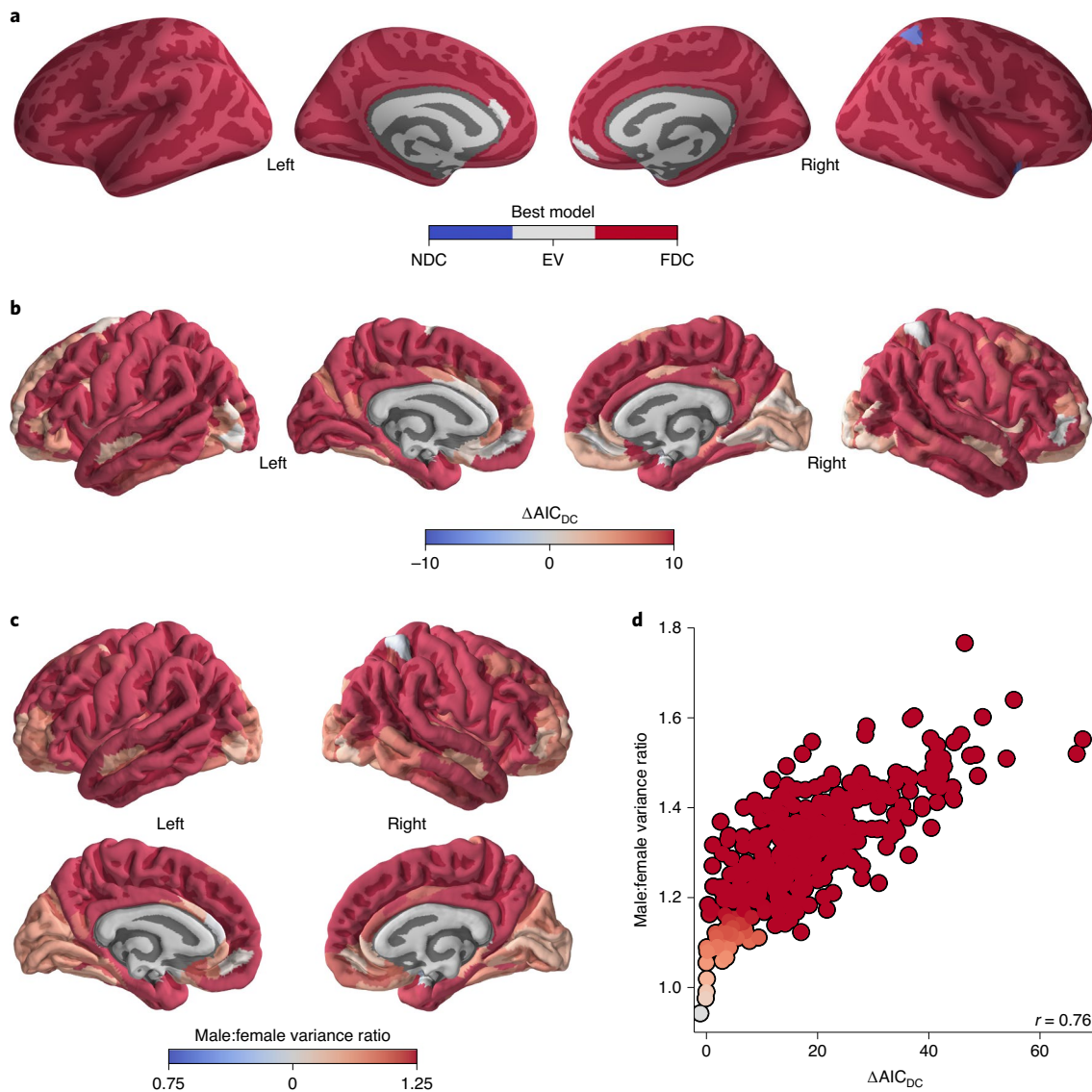


Fig. 1 | Regional patterning of X-chromosome dosage compensation and links to sex differences in anatomical variance for cortical SA. **a**, Categorical map showing the best-fitting X-chromosome dosage compensation model for each cortical region. NDC, no dosage compensation, EV, equal variance, FDC, full dosage compensation. **b**, Continuous map showing regional variation in the strength of statistical evidence for X-chromosome dosage compensation on SA, as indexed by ΔAIC_{DC} (Methods). ΔAIC_{DC} equals zero when the EV model fits best, and departures from zero reflect quantitative evidence for either NDC or FDC. $\Delta AIC_{DC} \leq -10$ is indicative of strong evidence for NDC while $\Delta AIC_{DC} \geq 10$ is indicative of strong evidence for FDC. Any values less than -10 or greater than 10 were set to -10 and 10 , respectively, for illustration. **c**, Continuous map showing regional variation in the magnitude of sex differences in SA phenotypic variance. **d**, Scatter plot of inter-regional variation in evidence for FDC (ΔAIC_{DC}) and the magnitude of sex biases in SA phenotypic variance (male:female variance ratio).

widespread for regional SA than regional CT and that XIs on regional CV are more a function of XIs on SA than CT.

After correcting for multiple comparisons within each phenotype (that is, SA, CT and CV) across all 358 cortical ROIs, we identified 75 regional measures with significant XI enrichment (that is, XI Z-statistic significantly > 0 ; Supplementary Tables 2–5), 56 (75%) of which were regional measures of SA. In contrast, 93 regional cortical measures showed significant XI depletion (that is, XI Z-statistic significantly < 0 ; Supplementary Tables 2–5), and the majority of these were regional measures of CT (Extended Data Figs. 7 and 8). Notably, the medial occipital visual cortices represented a concentrated locus of significant depletion of XIs for both primary dimensions of the cortical sheet (SA and CT) and their product (CV) (Extended Data Fig. 8). Thus, we observed robust statistical

evidence for enriched XIs on human neuroanatomical variation, and this effect was most apparent for the relative SA in specific sub-regions of the cortical sheet centered on the bilateral sensorimotor, the temporoparietal junction, the medial parietal and medial temporal cortices, the right inferior frontal and medial prefrontal cortices, and the left dorsolateral prefrontal cortex (Fig. 2d,e and Extended Data Fig. 8).

We took four complementary approaches to assess the reproducibility of our findings for XIs on regional SA. First, we compared spatial patterning of the XI Z-statistic for regional SA between the first and second releases of the UKB neuroimaging data and found this to show moderate reproducibility (cross-ROI Pearson's correlation in XI Z-statistics between the two releases: $r = 0.52$; Extended Data Fig. 9a). This compares favorably with the spatial reproduc-

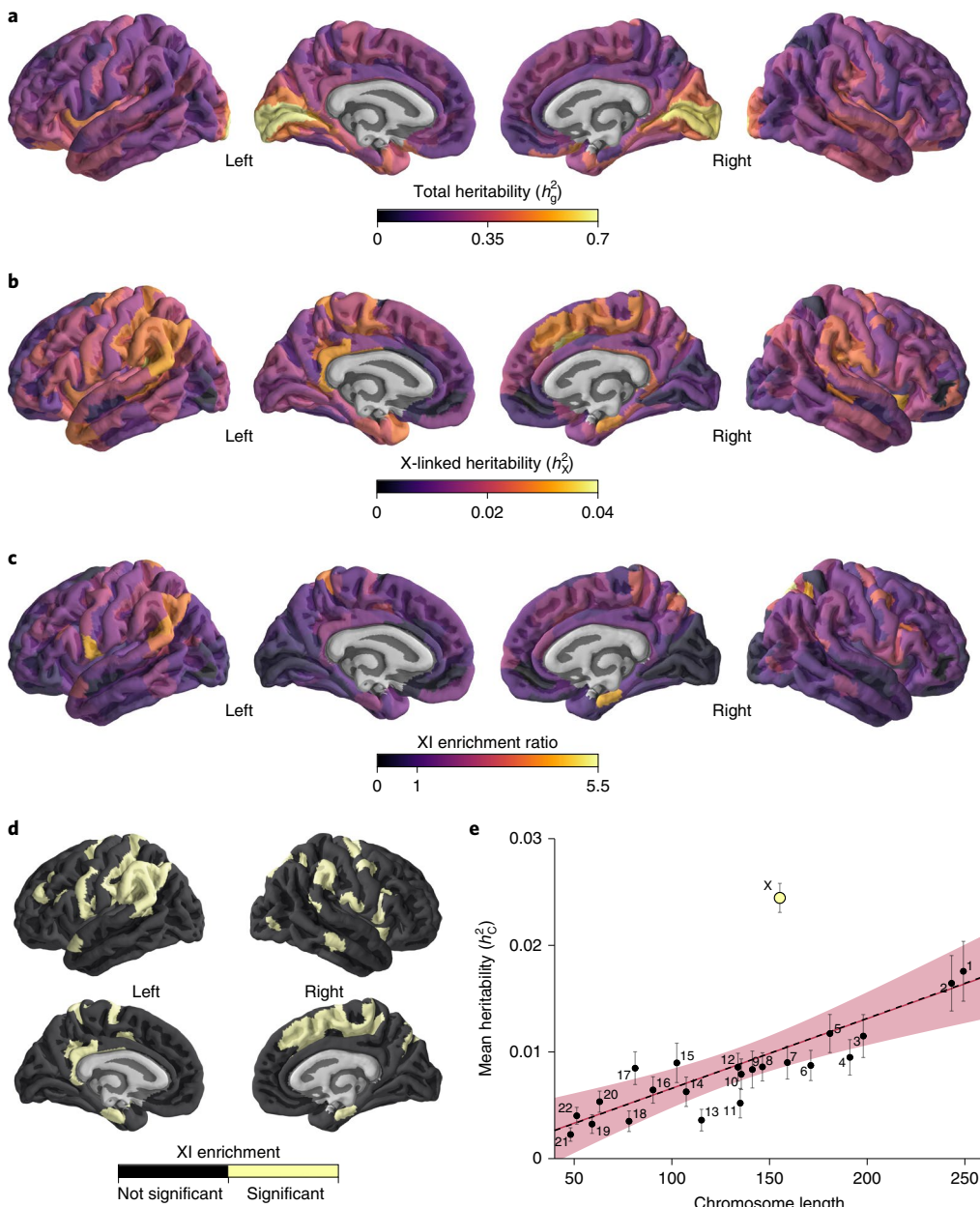


Fig. 2 | Regional patterning of XIs on cortical SA. **a**, Continuous map of total SNP heritability (h_g^2) for regional SA. **b**, Continuous map of X-linked heritability (h_X^2) for regional SA. **c**, Continuous map of the regional ratio between the observed proportion of total heritability assigned to the X-chromosome and the expected proportion from X-chromosome size (the XI enrichment ratio). Values greater than one reflect enriched XIs and values less than one reflect depleted XIs. **d**, Categorical map showing regions with significant enrichment of XIs. **e**, Scatter plot of the mean heritability per chromosome (h_c^2) plotted against chromosomal length for regional SA phenotypes with significantly enriched XIs ($n=56$ regions). The 23 data points correspond to the mean h_c^2 estimate of chromosomes across those regions (with accompanying 95% CIs). The line of best fit is displayed in red (with the accompanying 95% CI presented as a band), while the theoretical null is displayed as a dashed black line.

ibility seen for associations between behavior and regional brain anatomy, for example, see ref.²⁴. Second, we quantified cross-ROI correlations in the XI Z-statistic for SA between 100 randomly generated split-halves of the full UKB sample. The mean cross-ROI Pearson's correlation in XI Z-statistics across the split-half analyses was $r=0.55$ (Extended Data Fig. 9b). Third, we confirmed that the spatial patterning of observed XI Z-statistics was highly reproducible when GREML analyses were re-run using a more conservative minor allele frequency (MAF) threshold (cross-ROI $r=0.96$; Extended Data Fig. 9c). Fourth, to assess parcellation effects, we also computed regional XI for SA using an alternative cortical

parcellation scheme that has been extensively used in prior work, and divides the cortex into 308 similarly sized subdivisions of ROIs from the gyral-based Desikan–Killiany parcellation²⁵ (henceforth, termed 308-parcellation). This alternative parcellation scheme also provides access to a validated ‘spin’-based technique for comparing the spatial similarity between two cortical features^{26,27} (Methods). We projected regional XI Z-statistics for SA from the HCP-parcellation (Fig. 2c) into the 308-parcellation (Methods) and confirmed that the spatial distribution of XIs from this map was highly similar to XI Z-statistics computed within the 308-parcellation itself (cross-ROI $r=0.76$, $P_{\text{spin}} < 1 \times 10^{-4}$; Extended Data Fig. 9d,e).

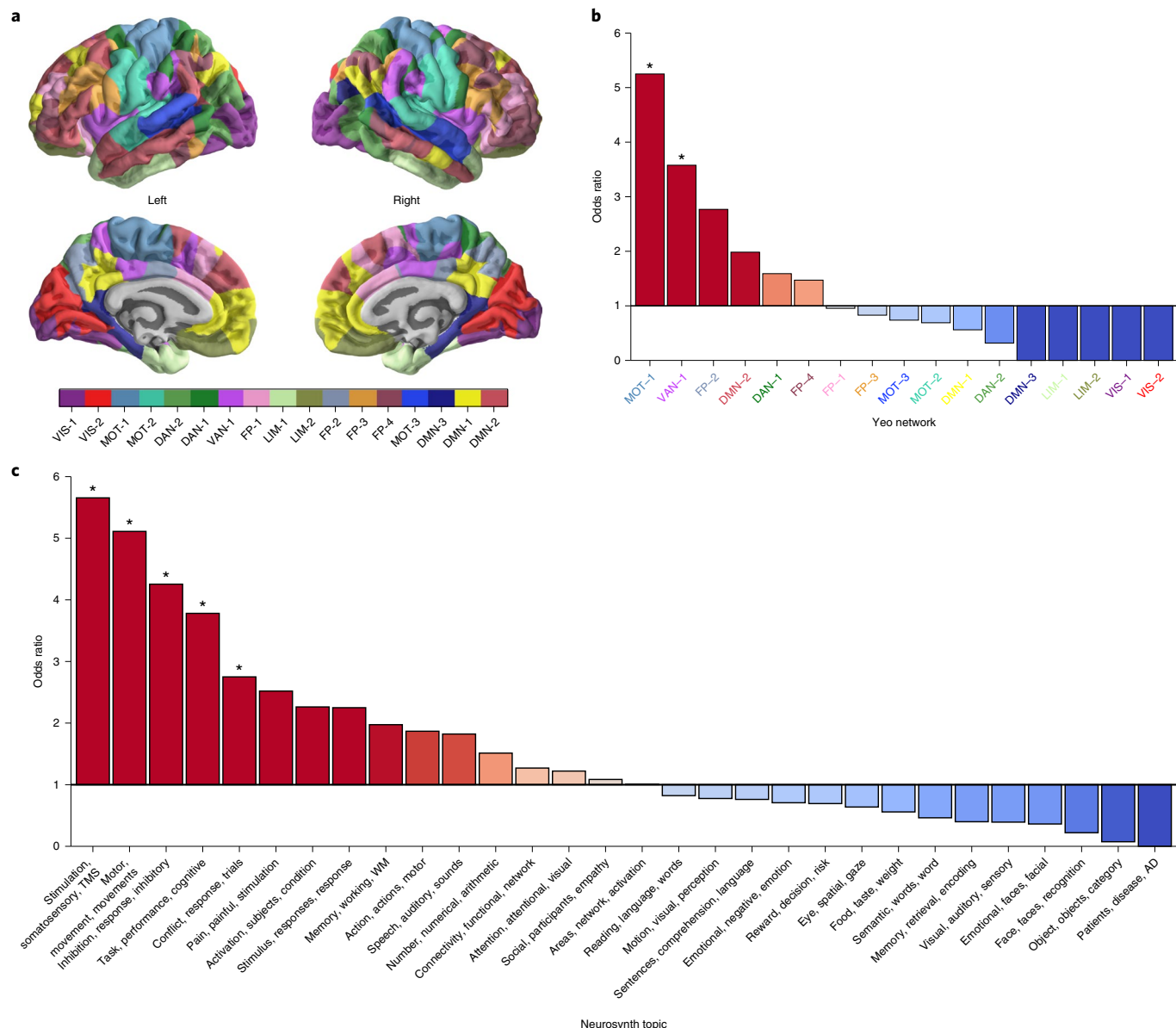


Fig. 3 | Topographic annotation of XIIs on cortical SA. **a**, Categorical map of 17 canonical resting-state functional connectivity networks as defined by Yeo, Krienen et al.²⁸. **b**, Bar chart illustrating the degree of spatial overlap between regions of significant XI enrichment for SA and each of the 17 Yeo-Krienen networks. **c**, Bar chart illustrating the degree of spatial overlap between regions of significant XI enrichment for SA and each of the 30 Neurosynth topics. **b,c**, Odds ratios greater than one indicate greater than chance overlap between regions of significantly enriched XIIs on SA and the Yeo-Krienen or Neurosynth feature in question. Asterisks denote $P_{\text{spin}} \leq 0.01$ in post hoc tests (Methods). $P_{\text{spin}} = 6.3 \times 10^{-3}$ and 8.6×10^{-3} for MOT-1 and VAN-1 in **b**; $P_{\text{spin}} = 7 \times 10^{-4}$, 1.6×10^{-3} , $<1 \times 10^{-4}$, 4×10^{-3} and 1×10^{-2} for somatosensory, motor, response inhibition, cognitive performance and conflict response topics, respectively, in **c**.

Topographic annotation of enriched XIIs on cortical SA. Taken together, the findings above indicate that SNP-based variation on the X-chromosome exerts a disproportionately large influence on SA variation in a specific subset of cortical regions (Fig. 2c,d). We hypothesized that the spatial patterning of enriched XIIs on SA may align with functional topography of the cortical sheet. To test this notion, we harnessed the 308-parcellation-based map of regional XIIs on SA (Extended Data Fig. 9d) to access spin-based methods^{26,27} to directly compare the spatial distribution of XI effects on cortical SA against cortical annotations from independent functional neuroimaging data^{28,29} (Methods).

We first asked whether the spatial distribution of XIIs on SA was organized in a non-random manner relative to the topography of canonical resting-state functional connectivity networks in

the human brain (as defined by the well-validated Yeo-Krienen-17-parcellation²⁸; Methods). The assignment of cortical ROIs from the 308-parcellation to network labels from the Yeo-Krienen-17 atlas explained a significantly large proportion of inter-regional variation in XIIs for SA (compared to 10,000 spins of these assignments, omnibus $F_{\text{observed}} = 5.9$, $P_{\text{spin}} = 0.01$). We further characterized this significant omnibus alignment between regional XI enrichment for SA and functional connectivity networks with post hoc overlap tests for each of the network components contained within the Yeo-Krienen-17-parcellation. The following six network components overlapped regions of significant XI enrichment for SA with an odds ratio > 1: one subcomponent of the motor network; two subcomponents from the frontoparietal network; and individual subcomponents from the ventral

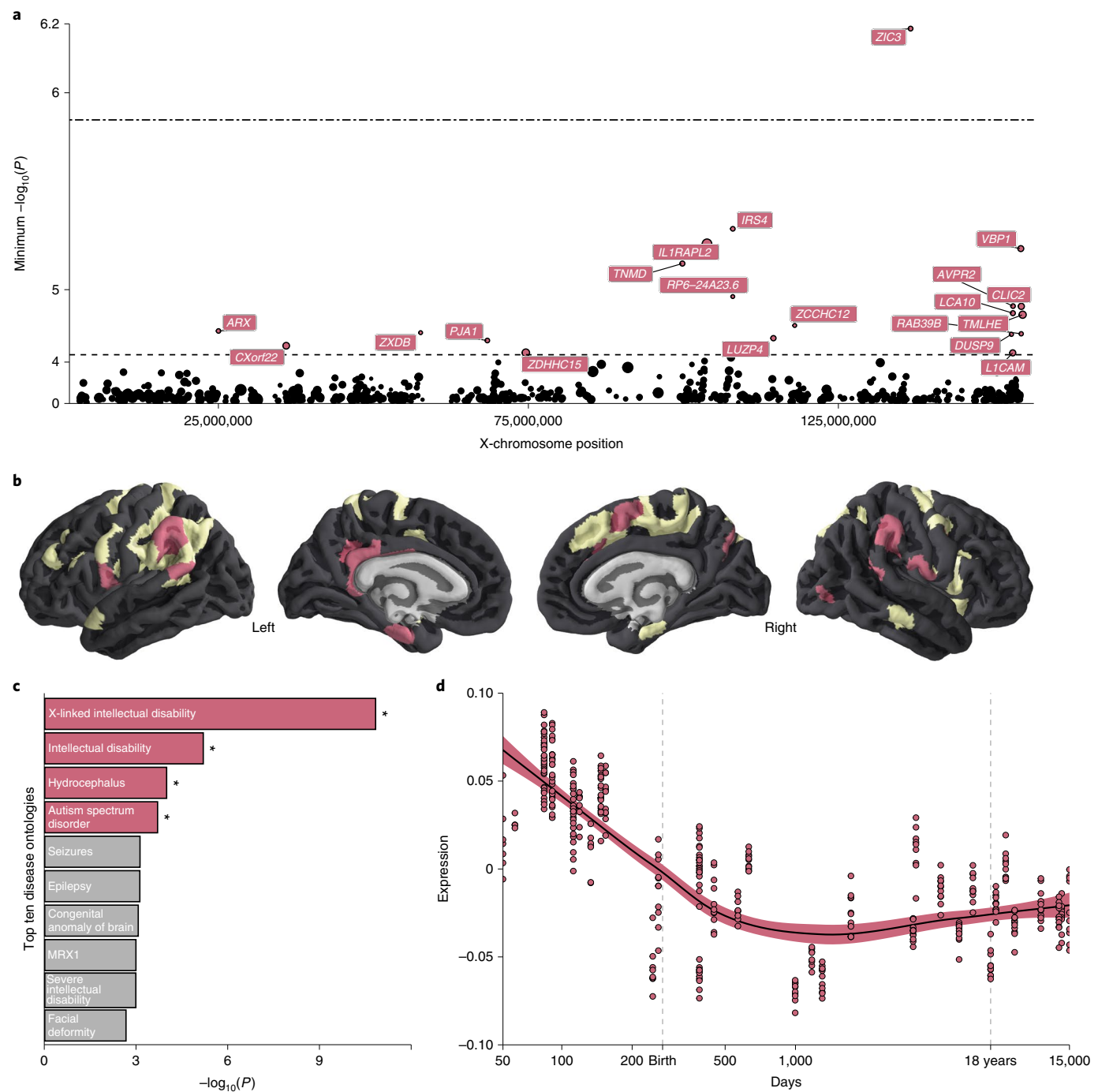


Fig. 4 | X-linked genes associated with regional SA phenotypes with enriched XIIs. **a**, X-chromosome-wide Manhattan plot of the minimum P value for each gene across all tested phenotypes. The x axis refers to the chromosomal position, the y axis refers to the significance of the gene-based association test as a $-\log_{10}(P)$ value, the horizontal dashed line denotes X-chromosome-wide significance ($P=6.91\times 10^{-5}$), and the horizontal two-dashed line denotes a more conservative significance threshold accounting for all tested phenotypes ($P=1.23\times 10^{-6}$). To improve readability, the y axis has been exponentiated, giving more space to significant genes and permitting the inclusion of gene labels. Circle size corresponds to the number of tested SNPs in each gene. **b**, Categorical map of gene discovery, where black refers to regions that were not tested (that is, those with no significant XI enrichment), yellow refers to regions that were tested but did not identify any genes in the gene-based tests and red refers to regions with significant gene associations. **c**, Bar chart of the top ten enriched disease ontologies based on Enrichr analysis. Fisher's exact test was used to compute one-sided P values, which are plotted along the x axis on a $-\log_{10}$ scale. Asterisks and color denote significance after correcting for multiple comparisons. **d**, Smoothed line plot of gene set expression across developmental time in the PsychENCODE dataset for the 20 identified genes. The x axis refers to the age of the sample in days (on a \log_2 scale), the y axis refers to expression, and each data point refers to a brain sample.

attention, dorsal attention and default-mode networks ($P_{\text{spin}} < 0.01$ for one motor and one ventral attention subnetwork; Fig. 3a,b and Supplementary Table 6).

To annotate the topographical pattern of enriched XIIs on cortical anatomy using finer-grained distinctions between different aspects of human brain function, we also compared the map of significantly

Table 1 | X-chromosome genes associated with regional SA phenotypes

Gene	CHR	BP location	N_{SNPs}	N_{PAR}	N	P_{min}	ROI(s)	DDD	XCI
ARX	X	25021811:25034065	6	3	33670	2.80×10^{-5}	lh_l_d23ab	Yes	No call
AVPR2	X	153167985:153172620	7	2	33770	1.43×10^{-5}	lh_l_43	No	Discordant
CLIC2	X	154505500:154563966	68	4	33756	1.44×10^{-5}	rh_r_pf	Yes	Mostly subject to XCI
CXorf22	X	35937851:36008269	114	6	33703	4.70×10^{-5}	lh_l_rsc	No	No call
DUSP9	X	152907946:152916781	3	2	33535	3.12×10^{-5}	rh_r_stv	No	Subject to XCI
IL1RAPL2	X	103810996:105011822	1114	55	33648	4.60×10^{-6}	rh_r_pf	No	Discordant
IRS4	X	107975712:107979651	7	2	33847	3.75×10^{-6}	rh_r_v4t	No	Mostly subject to XCI
L1CAM	X	153126969:153174677	61	9	33608	6.34×10^{-5}	rh_r_a32pr	Yes	Mostly escape from XCI
LCA10	X	153146127:153154444	13	3	33476	1.70×10^{-5}	rh_r_a32pr	No	Not applicable
LUZP4	X	114524293:114542121	20	5	33689	3.56×10^{-5}	rh_r_pef	No	No call
PJA1	X	68380694:68385636	7	3	33753	3.86×10^{-5}	rh_r_pos2	No	Subject to XCI
RAB39B	X	154487526:154493874	4	2	33831	3.07×10^{-5}	rh_r_pf	Yes	Subject to XCI
RP6-24A23.6	X	107965300:107975917	2	1	33789	1.15×10^{-5}	lh_l_31pd	No	Not applicable
TMLHE	X	154719776:154899605	196	8	33757	1.77×10^{-5}	rh_r_pf	No	Subject to XCI
TNMD	X	99839799:99854882	15	5	33688	6.23×10^{-6}	lh_l_stv	No	No call
VBP1	X	154425284:154468098	51	9	33704	4.94×10^{-6}	lh_l_31pd, rh_r_pf	No	Subject to XCI
ZCCHC12	X	117957753:117960931	2	1	33392	2.37×10^{-5}	lh_l_ec	No	Subject to XCI
ZDHHC15	X	74588262:74743337	262	10	33806	6.31×10^{-5}	rh_r_scef	Yes	Subject to XCI
ZIC3	X	136648301:136659850	9	3	33754	6.50×10^{-7}	lh_l_pf, rh_r_op4, rh_r_pf	Yes	Subject to XCI
ZXDB	X	57618269:57623906	2	1	33817	2.96×10^{-5}	rh_r_v4t	No	Subject to XCI

BP, base pair; CHR, chromosome; DDD, whether the gene has been linked to developmental disorders in the DDD project^{32,33}; N_{PAR} , number of effective parameters in the MAGMA gene-based test; N_{SNPs} , number of SNPs in the MAGMA gene-based test; P_{min} , minimum P value for a gene across SA area phenotypes; ROI(s), region(s) of interest (in the HCP-parcellation) with significant gene-based association; XCI, X-chromosome inactivation status in Balaton et al.⁴³.

enriched XIIs on SA with 30 different meta-analytic maps of cortical activation from Neurosynth^{29,30} (Methods). These 30 maps span the gamut of cognitive constructs (or ‘topics’) examined across >11,000 individual functional neuroimaging studies contained within the Neurosynth database³⁰ (Supplementary Table 7). We observed a significant omnibus alignment between the spatial patterning of these 30 Neurosynth topic maps and regional XI enrichment for SA (mean $F_{observed} = 9.3$, $P_{spin} = 0.02$; Methods). Post hoc analysis identified 16 Neurosynth topic maps that overlapped regions of significant XI enrichment for SA with an odds ratio > 1, the following five of which were significant at $P_{spin} \leq 0.01$: somatosensory, motor, response inhibition, conflict response and cognitive performance (Fig. 3c, Supplementary Table 7 and Methods).

Thus, our comparison with two complementary functional annotations of the cortical sheet suggests that enriched XIIs on SA tend to be concentrated in a subset of functional systems within the cerebral cortex, including the following: (1) a somatomotor system encompassing primary sensory, primary and supplemental motor, and insular regions; (2) a response–inhibition system centered on the inferior frontal gyrus; and (3) higher-order attentional and default-mode systems centered on the temporoparietal junction.

Genomic annotation of enriched XIIs on SA. To identify which specific genes might be relevant to the observed enriched XIIs on human brain anatomy, we conducted a series of gene-based XWA analyses in each of the 56 cortical SA phenotypes that exhibited significant XI enrichment (Methods). Briefly, we observed substantial inflation of the gene-based test statistics for these phenotypes (median gene-based $\lambda_{GC} = 1.36$ (IQR = 1.25–1.48)), which

is indicative of a robust polygenic signal on the X-chromosome (but could also reflect remaining population stratification despite our control for this in the analysis). Next, to synthesize results across the enrichment map, we calculated the minimum P value for each gene across all particular ROIs (Fig. 4a, with results of SNP-based association testing provided in Extended Data Fig. 10). This yielded a list of 20 X-chromosome genes that met the threshold of X-chromosome-wide significance for gene-based testing ($P = 6.91 \times 10^{-5}$) across the cortex (Table 1 and Fig. 4b), and one gene (ZIC3) that met the stricter significance threshold correcting for all phenotypes tested ($P = 1.23 \times 10^{-6}$).

Biological annotation of the 20 X-linked genes implicated by XWA for regional SA revealed significant enrichment of these genes in the following four disease ontologies: X-linked intellectual disability, intellectual disability, hydrocephalus and autism spectrum disorder (Fig. 4c and Methods). Of note, the enrichment for X-linked intellectual disability is likely reflective of the fact that this annotation is defined by X-linkage status, which was shared by all the genes we submitted to overrepresentation analysis against a genome-wide background gene set. However, this caveat does not apply to other significant disease annotation enrichments. We also independently verified that—after restricting the analysis to only those genes that are expressed in the human brain per the Human Protein Atlas³¹—XWA significant genes were significantly enriched among a manually curated list of genes showing probable or confirmed associations with developmental disabilities by the Deciphering Developmental Disorders (DDD) project^{32,33} (hypergeometric $P = 3.24 \times 10^{-3}$; Methods). Taken together, these analyses indicate that relative to all other brain-expressed genes, those

X-linked genes highlighted in our gene-based XWA analyses are enriched for those that can cause neurodevelopmental disorders when mutated. We did not find that XWA-implicated genes were significantly enriched for DDD target genes relative to all other brain-expressed X-chromosome genes (hypergeometric $P=0.1$). In keeping with these disease enrichments for disorders with early developmental roots, we found that this set of X-linked genes were most highly expressed in cortical tissue during prenatal life in the PsychENCODE dataset³⁴ (Fig. 4d and Methods). Thus, both topographic (Fig. 3) and genomic (Fig. 4) annotations of enriched XIs on human cortical anatomy converge to highlight a concentration of XIs on brain circuits and genes that are important for adaptive behavior.

Discussion

Our study advances the understanding of genetic influences on human neuroanatomical variation in four key directions, with several implications for neuroscientific theory and practice.

First, we provide novel evidence from quantitative genetics for X-chromosome dosage compensation effects on human brain anatomy. This evidence is detectable for the majority of structural traits examined, which is in line with evidence for X-chromosome inactivation from molecular genetics⁶. Thus, common X-linked genetic variation tends to account for a greater proportion of phenotypic variation in brain anatomy among males compared to females. This hitherto unknown sex difference in the genetic architecture of human neuroanatomical variation echoes the male-biased penetrance of rare X-linked variation for intellectual disability⁸. Both of these phenomena could be explained by the monoallelic status of X-linked genes in males and resultant unmasking of recessive allele effects in males⁸ combined with invariance in X-chromosome parent of origin across male tissues versus the potential for mixed contribution of maternally and paternally inherited X-chromosome alleles in females⁶. Such mechanisms have also been proposed to contribute to greater overall phenotypic variance in the heterogametic sex of species with chromosomal sex-determination systems (XY males in eutherian mammals, and ZW females in birds and butterflies)³⁵. Our study provides new empirical support for this idea by showing that cortical regions with a larger male bias in SA variance tend to show stronger evidence of full X-chromosome dosage compensation. However, it is important to note that the small size of the X-chromosome partition means that even large sex differences in common X-linked genetic variance cannot be the sole source of those sex differences in overall phenotypic variance observed for cortical SA. An important goal for future work would be to develop approaches to estimate Y-chromosome influences on trait variation, and ask how these relate to those from the X-chromosome, especially for traits with sex-biased means or variances.

Second, by partitioning total heritability into X-linked and autosomal compartments, we directly quantified the information that can be lost by failing to consider the X-chromosome in genomic studies of brain-related phenotypes⁵. The observation that this 5% portion of the genome can account for over 20% of SNP-based heritability for some traits is particularly sobering. We note that the true magnitudes of trait heritability lost by excluding the X-chromosome are likely to be larger than the estimates provided by our study design, which excludes rare genetic variation, non-additive genetic effects and pseudoautosomal regions of the X-chromosome³⁶. Nevertheless, our findings from the GREML analysis provide new quantitative genetic support for prior theories from earlier transcriptomic⁷ and clinical⁸ data that predicted an enriched influence of the X-chromosome on neurodevelopmental traits.

Third, we show that enriched XIs on human brain anatomy appear to be focused on particular morphometric properties. Observed XIs on global measures of brain anatomy, such as total brain volume, total SA and overall mean CT, are in fact

significantly smaller than would be predicted from the size of the X-chromosome partition, and we failed to detect evidence for enriched XIs for any regional measure of CT (with the sole exception of an isolated region within the left premotor cortex (area 6d)¹⁴). In contrast, XIs are markedly enriched for relative SA in several regions of the cortical sheet (which translates into enriched XIs on several measures of regional CV). This morphometric selectivity suggests that enriched XIs on the developing brain are likely to be operating on one or more of the biological processes that are capable of shaping local SA independently of global SA³⁷. Such processes include morphogen gradients, local rates of neuronal progenitor pool division, the degree of tangential radial migration during neuronal population of the cortical plate and the spatial patterning of thalamocortical inputs³⁸.

Fourth, to put our findings in a richer biological context, we combined two complementary approaches for annotation of observed enriched XIs on regional cortical SA: (1) comparison of the enriched XI map with independently generated functional annotations of the cortical sheet and (2) XWA analyses that identify specific X-linked genes influencing regional SA. Using recently developed surface-based methods for functional annotation of cortical maps^{26,27}, we showed that enriched XIs on regional cortical SA are overrepresented within cortical systems involved in motor control, decision-making and attention. These annotational results do not directly demonstrate a relevance of XIs on SA for inter-individual variation in brain function but provide an anatomical context for orthogonal evidence from XWA analyses. Specifically, several of the X-linked genes we found to be linked to SA variation are known to cause intellectual disability when mutated in humans. For example, *RAB39B* encodes a GTPase that is involved in vesicular trafficking, is associated with X-linked intellectual disability, autism spectrum disorder and macrocephaly when mutated, and is thought to be involved in neurogenesis, neuronal fate and regulation of brain development³⁹. Another X-linked intellectual disability risk gene identified by our XWA analyses is *L1CAM*, which encodes an axonal glycoprotein with roles in neuronal migration and differentiation⁴⁰. The association of enriched XIs with cortical systems and genes that are important for adaptive behavior is consistent with evolutionary theories regarding enrichment of the X-chromosome for genes influencing traits that are important for reproductive fitness⁴¹. Specifically, as the X-chromosome is hemizygous in XY males, it has been theorized that X-linked variation should be subject to strong negative and positive selection for alleles that reduce and enhance reproductive fitness, respectively⁴². In this context, it is notable that some of our topographic and genomic annotations linked enriched XIs on SA to higher-order cognitive processes that may be particularly important for reproductive competitiveness in humans⁸.

Taken together, our findings suggest that the very chromosome that has been conspicuously excluded from large-scale imaging genetic research in fact exerts a conspicuously large influence on several aspects of human brain anatomy. Moreover, we show that this influence is sex biased in its magnitude and involves both brain networks and genes that are known to be relevant for adaptive function in humans.

Online content

Any methods, additional references, Nature Research reporting summaries, source data, extended data, supplementary information, acknowledgements, peer review information; details of author contributions and competing interests; and statements of data and code availability are available at <https://doi.org/10.1038/s41593-021-00890-w>.

Received: 4 June 2020; Accepted: 14 June 2021;
Published online: 22 July 2021

References

1. Grasby, K. L. et al. The genetic architecture of the human cerebral cortex. *Science* **367**, eaay6690 (2020).
2. Biton, A. et al. Polygenic architecture of human neuroanatomical diversity. *Cereb. Cortex* **30**, 2307–2320 (2020).
3. Zhao, B. et al. Genome-wide association analysis of 19,629 individuals identifies variants influencing regional brain volumes and refines their genetic co-architecture with cognitive and mental health traits. *Nat. Genet.* **51**, 1637–1644 (2019).
4. Smith, S. M. et al. An expanded set of genome-wide association studies of brain imaging phenotypes in UK Biobank. *Nat. Neurosci.* **24**, 737–745 (2021).
5. Wise, A. L., Gyi, L. & Manolio, T. A. eXclusion: toward integrating the X chromosome in genome-wide association analyses. *Am. J. Hum. Genet.* **92**, 643–647 (2013).
6. Lyon, M. F. Gene action in the X-chromosome of the mouse (*Mus musculus* L.). *Nature* **190**, 372–373 (1961).
7. Nguyen, D. K. & Disteche, C. M. Dosage compensation of the active X chromosome in mammals. *Nat. Genet.* **38**, 47–53 (2006).
8. Zechner, U. et al. A high density of X-linked genes for general cognitive ability: a run-away process shaping human evolution? *Trends Genet.* **17**, 697–701 (2001).
9. Raznahan, A. et al. Globally divergent but locally convergent X- and Y-chromosome influences on cortical development. *Cereb. Cortex* **26**, 70–79 (2016).
10. Yang, J. et al. Genome partitioning of genetic variation for complex traits using common SNPs. *Nat. Genet.* **43**, 519–525 (2011).
11. Yang, J., Lee, S. H., Goddard, M. E. & Visscher, P. M. GCTA: a tool for genome-wide complex trait analysis. *Am. J. Hum. Genet.* **88**, 76–82 (2011).
12. Fischl, B. et al. Whole brain segmentation: automated labeling of neuroanatomical structures in the human brain. *Neuron* **33**, 341–355 (2002).
13. Fischl, B. et al. Automatically parcellating the human cerebral cortex. *Cereb. Cortex* **14**, 11–22 (2004).
14. Glasser, M. F. et al. A multi-modal parcellation of human cerebral cortex. *Nature* **536**, 171–178 (2016).
15. Lerch, J. P. et al. Studying neuroanatomy using MRI. *Nat. Neurosci.* **20**, 314–326 (2017).
16. Hofer, E. et al. Genetic correlations and genome-wide associations of cortical structure in general population samples of 22,824 adults. *Nat. Commun.* **11**, 4796 (2020).
17. Matoba, N., Love, M. I. & Stein, J. L. Evaluating brain structure traits as endophenotypes using polygenicity and discoverability. *Hum. Brain Mapp.* <https://doi.org/10.1002/hbm.25257> (2020).
18. Forde, N. J. et al. Sex differences in variability of brain structure across the lifespan. *Cereb. Cortex* **30**, 5420–5430 (2020).
19. Ritchie, S. J. et al. Sex differences in the adult human brain: evidence from 5216 UK Biobank participants. *Cereb. Cortex* **28**, 2959–2975 (2018).
20. Finucane, H. K. et al. Partitioning heritability by functional annotation using genome-wide association summary statistics. *Nat. Genet.* **47**, 1228–1235 (2015).
21. van der Meer, D. et al. Quantifying the polygenic architecture of the human cerebral cortex: extensive genetic overlap between cortical thickness and surface area. *Cereb. Cortex* **30**, 5597–5603 (2020).
22. Evans, L. M. et al. Comparison of methods that use whole genome data to estimate the heritability and genetic architecture of complex traits. *Nat. Genet.* **50**, 737–745 (2018).
23. Ge, T. et al. Phenome-wide heritability analysis of the UK Biobank. *PLoS Genet.* **13**, e1006711 (2017).
24. Kharabian Masouleh, S., Eickhoff, S. B., Hoffstaedter, F., Genon, S. & Alzheimer's Disease Neuroimaging Initiative. Empirical examination of the replicability of associations between brain structure and psychological variables. *eLife* **8**, e43464 (2019).
25. Romero-Garcia, R., Atienza, M., Clemmensen, L. H. & Cantero, J. L. Effects of network resolution on topological properties of human neocortex. *NeuroImage* **59**, 3522–3532 (2012).
26. Alexander-Bloch, A. F. et al. On testing for spatial correspondence between maps of human brain structure and function. *NeuroImage* **178**, 540–551 (2018).
27. Vásá, F. et al. Adolescent tuning of association cortex in human structural brain networks. *Cereb. Cortex* **28**, 281–294 (2017).
28. Yeo, B. T. T. et al. The organization of the human cerebral cortex estimated by intrinsic functional connectivity. *J. Neurophysiol.* **106**, 1125–1165 (2011).
29. Yarkoni, T., Poldrack, R. A., Nichols, T. E., Van Essen, D. C. & Wager, T. D. Large-scale automated synthesis of human functional neuroimaging data. *Nat. Methods* **8**, 665–670 (2011).
30. Rubin, T. N. et al. Decoding brain activity using a large-scale probabilistic functional-anatomical atlas of human cognition. *PLoS Comput. Biol.* **13**, e1005649 (2017).
31. Sjöstedt, E. et al. An atlas of the protein-coding genes in the human, pig, and mouse brain. *Science* **367**, eaay5947 (2020).
32. Deciphering Developmental Disorders Study. Prevalence and architecture of de novo mutations in developmental disorders. *Nature* **542**, 433–438 (2017).
33. Martin, H. C. et al. The contribution of X-linked coding variation to severe developmental disorders. *Nat. Commun.* **12**, 627 (2021).
34. Li, M. et al. Integrative functional genomic analysis of human brain development and neuropsychiatric risks. *Science* **362**, eaat7615 (2018).
35. Reinhold, K. & Engqvist, L. The variability is in the sex chromosomes: brief communication. *Evolution* **67**, 3662–3668 (2013).
36. Young, A. I. Solving the missing heritability problem. *PLoS Genet.* **15**, e1008222 (2019).
37. Schmitt, J. E. et al. A comprehensive quantitative genetic analysis of cerebral surface area in youth. *J. Neurosci.* **39**, 3028–3040 (2019).
38. Cadwell, C. R., Bhaduri, A., Mostajo-Radji, M. A., Keefe, M. G. & Nowakowski, T. J. Development and arealization of the cerebral cortex. *Neuron* **103**, 980–1004 (2019).
39. Woodbury-Smith, M. et al. Mutations in *RAB39B* in individuals with intellectual disability, autism spectrum disorder, and macrocephaly. *Mol. Autism* **8**, 59 (2017).
40. Kenrick, S., Watkins, A. & De Angelis, E. Neural cell recognition molecule L1: relating biological complexity to human disease mutations. *Hum. Mol. Genet.* **9**, 879–886 (2000).
41. Graves, J. A. M., Gécz, J. & Hameister, H. Evolution of the human X—a smart and sexy chromosome that controls speciation and development. *Cytogenet. Genome Res.* **99**, 141–145 (2002).
42. Vallender, E. J. & Lahn, B. T. How mammalian sex chromosomes acquired their peculiar gene content. *Bioessays* **26**, 159–169 (2004).
43. Balaton, B. P. et al. Derivation of consensus inactivation status for X-linked genes from genome-wide studies. *Biol. Sex Differ.* **6**, 35 (2015).

Publisher's note Springer Nature remains neutral with regard to jurisdictional claims in published maps and institutional affiliations.

This is a U.S. government work and not under copyright protection in the U.S.; foreign copyright protection may apply 2021

Methods

The UKB sample. The UKB is a large-scale biomedical study designed to investigate the influence of genetic and environmental variables on human health and well-being⁴⁴. All participants provided informed consent, were genotyped and completed a myriad of questionnaires related to complex traits. A subset of participants also took part in a MRI protocol, where they attended a scanning appointment at one of three sites. Following exclusions described below, the sample size for the present study was 32,256 (52.97% female, mean age = 64.31 years). Data and materials are available via UKB (<https://www.ukbiobank.ac.uk>).

Image acquisition and preparation. Detailed information regarding the UKB image acquisition process is available from the UKB website (https://biobank.ctsu.ox.ac.uk/crystal/crystal/docs/brain_mri.pdf). Imaging data were downloaded on 23 April 2020. T1-weighted and T2 FLAIR structural scans were acquired on identical Siemens Skyra 3T scanners. For T1-weighted imaging, a 3D MPAGE sequence was used with 1-mm sagittal slices, 1×1-mm in-plane resolution, in-plane acceleration iPAT = 2 and prescan normalization. For T2 FLAIR imaging, a 3D SPACE sequence was used with 1.05-mm sagittal slices, 1×1-mm in-plane resolution, in-plane acceleration iPAT = 2, partial Fourier = 7/8, fat saturation, elliptical k-space scanning and prescan normalization⁴⁵.

We used the PreFreeSurfer and FreeSurfer pipelines from the HCP pipeline (v.3)⁴⁶ (<https://github.com/Washington-University/HCPpipelines>) for the data pre-processing of the T1-weighted and T2 FLAIR MRI scans. The PreFreeSurfer pipeline corrected gradient nonlinearity distortion and aligned the T1-weighted and T2 FLAIR images. The FreeSurfer pipeline used FreeSurfer (v.5.3.0)⁴⁷ software (<https://surfer.nmr.mgh.harvard.edu>) for the surface reconstruction from the T1-weighted images. Briefly, the cortical surface for each participant was reconstructed using the following steps: skull stripping⁴⁸, segmentation of cortical gray and white matter⁴⁵; separation of the two hemispheres and subcortical structures^{12,13,49}; and, finally, construction of a smooth representation of the gray-white interface and the pial surface⁵⁰. To examine regional anatomical phenotypes, we used the multimodal HCP-parcellation¹⁴ as our primary parcellation of interest. An alternative gyral-based (that is, anatomically driven) 308-parcellation was used for sensitivity analysis and to implement spin-based map-alignment tests (see below). To define the 308 anatomical labels within this alternative parcellation, the 68 cortical regions in the Desikan–Killiany atlas⁵¹ were subparcellated into 308 spatially contiguous regions (152 for the left hemisphere, 156 for the right hemisphere) of approximately equal size (~5 cm²) using a backtracking algorithm as previously described²⁵. Both the HCP-parcellation and the 308-parcellation were generated once on the surface of the standard anatomical template (fsaverage) and subsequently transformed to the surface of each individual subject. The surface parcellation for each subject was then interpolated and expanded to their respective T1-weighted volume. Regional SA, CT and CV for each parcellation was computed using Freesurfer’s ‘mris_anatomical_stats’ command and subcortical volume for the standard ‘aseg’ subcortical parcellation was calculated using the ‘mri_segtstats’ command. Finally, regional measures were adjusted for their corresponding global phenotype (that is, regional CV for total brain volume, regional SA for total SA and regional CT for mean CT) separately within each sex before analysis.

Genotyping, imputation and quality control. Genotyping and imputation procedures were centrally performed by the original UKB investigators⁵². Genotype data for the autosomes and X-chromosome were phased and imputed using SHAPEIT⁵³ and IMPUTE⁴², respectively. For the X-chromosome, the pseudoautosomal regions and non-pseudoautosomal regions were phased and imputed independently, applying the same approach used for the autosomes. As the genotyping, haplotype estimation (phasing) and imputation procedures for all genetic markers have already been extensively described by the original UKB investigators, we refer the reader to their previously published study for further details⁵². Information regarding these procedures is also available at <https://www.ukbiobank.ac.uk/scientists-3/genetic-data>.

In the present study, we followed best practices for estimating heritability and applied additional quality control filters to this aim. First, using the quality control variables provided by the UKB investigators, we removed participants with putative sex chromosome aneuploidy (as the original UKB investigators inferred from the measured intensities of chromosomes X and Y)⁵², excessive heterozygosity (that is, poor quality genotype data) and mismatched self-reported sex and chromosomal sex. Next, we restricted the sample to participants of non-Hispanic European ancestry with processed neuroimaging data ($n=33,870$) to minimize the potential influence of population stratification. We then applied standard thresholds to the imputed variants, excluding those with (1) an imputation score of less than 0.30, (2) a MAF of less than 0.0003, (3) a Hardy–Weinberg equilibrium $P < 1 \times 10^{-6}$ and/or (4) three or more observed alleles (that is, multiallelic sites). We also excluded the pseudoautosomal regions from analysis as their very small size precluded a reliable estimation of partitioned heritability and statistical enrichment (and they cannot be merged with the non-pseudoautosomal region in GCTA). We note that imputation and MAF thresholds were established based on previous research on optimal parameters for estimating heritability from genomic data²².

The sample was then pruned for missingness, removing participants missing 5% or more of genotypes; however, no samples met this criterion after applying the

variant-level filters described above. In preparation for the heritability analyses, the sample was pruned for relatedness, removing one participant from a related pair if estimated relatedness exceeded 0.05 (note that the pruning algorithm selectively removed individuals to maximize the remaining sample size). This resulted in the removal of 1,606 participants. Finally, we removed eight participants who had values of zero for any of the regional phenotypes. These preprocessing steps yielded a final sample of 32,256 participants with information on 16,873,171 SNPs (16,255,343 autosomal SNPs and 617,828 X-chromosome SNPs) spanning the genome.

Genotype coding. The genetic analyses reported in this study were conducted using PLINK (v.2.00)⁵⁴ and GCTA (v.192.1beta6)¹¹. During quality control and preprocessing, imputed dosages were converted to genotype hard calls using the default settings in PLINK, where calls with an uncertainty greater than 0.10 were treated as missing. Both PLINK and GCTA handle the X-chromosome in a similar manner. In GCTA, the X-chromosome genetic relationship matrix (GRM) was constructed with females coded as diploid (0, 1 or 2) and males coded as homozygous diploid (0 or 2), as described below. The GRM was then parameterized under three different assumptions related to genetic variance on the X-chromosome (that is, dosage compensation), and the best-fitting model was selected (also described below). In PLINK, X-chromosome association analyses were conducted by analyzing males as homozygous diploid (0 or 2), which is in accordance with the evidence of full dosage compensation for those phenotypes.

GRMs. We used GCTA (v.1.92.1beta6) to construct autosomal and X-chromosome GRMs for the sample, which quantified genetic similarity between all individuals in the sample. First, the genetic relationship between individuals j and k was

$$\text{estimated as } A_{jk} = \frac{N}{N} \sum_{i=1}^N \frac{(x_{ij} - 2p_i)(x_{ik} - 2p_i)}{2p_i(1-p_i)}$$

for autosomal SNPs, where N refers to the number of SNPs and x and p refer to the number of copies (0, 1 or 2) and the frequency of the reference allele for SNP i . This equation was then modified to estimate the genetic relationship based on the X-chromosome that accounts for the fact that males have only one X-chromosome. As described by Yang and colleagues¹¹, the original equation was modified such that genetic relationships were estimated as $A_{jk}^F = \sum_{i=1}^N \frac{(x_{ij}^F - 2p_i)(x_{ik}^F - 2p_i)}{2p_i(1-p_i)}$ for a female–female pair,

$$A_{jk}^M = \sum_{i=1}^N \frac{(x_{ij}^M - p_i)(x_{ik}^M - p_i)}{p_i(1-p_i)}$$

for a male–male pair, and $A_{jk}^{FM} = \sum_{i=1}^N \frac{(x_{ij}^F - 2p_i)(x_{ik}^M - p_i)}{\sqrt{2p_i(1-p_i)}}$

GREML. We also used GCTA (v.1.92.1beta6) to estimate and partition total SNP-based heritability for the 1,091 morphological phenotypes via the GREML method. To estimate and partition heritability across the autosomes and the X-chromosome, we began with a single-component GREML analysis in GCTA. This mixed-linear model can be expressed as $\mathbf{y} = \mathbf{X}\boldsymbol{\beta} + \mathbf{g}_a + \boldsymbol{\epsilon}$ with $\text{var}(\mathbf{y}) = \mathbf{V} = A_a\sigma_a^2 + I\sigma_e^2$, where \mathbf{y} is a $n \times 1$ vector of standardized phenotypes with sample size n , $\boldsymbol{\beta}$ is a vector of fixed effects for covariates (here, sex, age, the first 20 principal components of ancestry, genotyping batch and scanning site), \mathbf{g}_a is a $n \times 1$ vector of genetic effects attributable to the autosomes, $\boldsymbol{\epsilon}$ is a vector of residual effects, A is a GRM that quantifies the genetic similarity between individuals in the sample, I is a $n \times n$ identity matrix and σ_a^2 is the variance explained by all autosomal SNPs. Following this model, the restricted maximum likelihood method was used to estimate σ_a^2 . Note that heritability estimates were derived from a model where variance component estimates were constrained to be greater than zero for the sake of interpretation, as negative variance estimates can skew the proportion of variance explained by SNPs in a given partition.

The basic model was then extended to estimate the variance explained by the X-chromosome (σ_X^2), such that $\mathbf{y} = \mathbf{X}\boldsymbol{\beta} + \mathbf{g}_a + \mathbf{g}_X + \boldsymbol{\epsilon}$, where \mathbf{g}_X is a vector of genetic effects attributable to the X-chromosome. To evaluate evidence of dosage compensation¹¹, we used GCTA to fit this mixed-linear model under three different assumptions for the variance of \mathbf{g}_X : (1) no dosage compensation, where variance equals $A_X^{\text{ND}}\sigma_X^2$; (2) full dosage compensation, where variance equals $A_X^{\text{FD}}\sigma_X^2$; and (3) equal variance for males and females, where variance equals $A_X^{\text{EF}}\sigma_X^2$. Model log likelihood (L) and Akaike information criterion (AIC) were used to identify the model that best fit the data. The latter was calculated as $AIC = -2L + 2k$, where L is the log likelihood and k is the number of parameters estimated in each model (note that k is invariant across models). Differences in AIC (ΔAIC) were then computed to further quantify the degree of evidence for the optimal model relative to the equal variance model (that is, the theoretical null model), where $\Delta AIC = \Delta AIC_{\text{EV}} - \Delta AIC_{\min}$. As established in information theory, a difference of ten or greater reflects strong evidence for the optimal model minimizing AIC ⁵⁵. Parameter estimates from the best fitting model were carried forth and used in subsequent analyses.

For the purposes of plotting and visualization, we also created a dimensional index of the degree of support for the possible dosage compensation models. Specifically, we adjusted the ΔAIC statistic by multiplying it by -1 when the best fitting model was the no dosage compensation model. As such, this modified statistic, which we call ΔAIC_{DC} , is equal to zero when the equal variance model fits best. Departures from zero reflect quantitative and dimensional evidence for either

no dosage compensation (negative values) or full dosage compensation (positive values). Accordingly, $\Delta\text{AIC}_{\text{DC}}$ values ≤ -10 are indicative of strong evidence for no dosage compensation while values $\geq +10$ are indicative of strong evidence for full dosage compensation.

Sex-stratified heritability analysis. To provide a complementary test of male–female differences in X-linked genetic variance, we used sex-stratified analyses to separately estimate heritability in males and females for the 920 cortical and subcortical ROIs where the full dosage compensation model fit best. In these sex-stratified GREML analyses, we employed the same procedure used to produce our final estimates of total and partitioned heritability, but we performed the analysis in a manner naïve to dosage compensation. A nonparametric Wilcoxon rank-sum test was then used to test whether the X-linked heritability estimates in female-only and male-only subsamples were similar distributions with equivalent medians. Finally, we calculated the ratio of the medians of this distribution and used bootstrapping to compute a 95% CI for this ratio.

Sex ratio of cortical SA variance. We calculated the phenotypic variance of cortical SA in males and females separately. To parallel the primary analysis, the regional SA phenotypes were adjusted for total SA, the first 20 principal components of ancestry, sex, age, genotyping batch and scanning site. The phenotypic variance ratio was then computed as $\frac{V_{\text{PM}}}{V_{\text{PF}}}$, where V_{PM} and V_{PF} refer to the phenotypic variance in males and females, respectively.

Enrichment tests. Here, we defined enrichment as the proportion of heritability in the partition divided by the proportion of genomic base pairs that reside on the partition, such that the XI ratio for a given phenotype is $\frac{(h_X^2/h_g^2)}{(\text{length}_X/\text{length}_g)}$. This definition is analogous to previous definitions of enriched heritability^{20,56}, and establishes a partition-specific null that follows the theoretical assumption of equal per-SNP heritability^{57,58}. To determine whether the observed heritability for a given partition was statistically different than what would be expected given its genomic length, we used a one-sample enrichment Z-test that was monotonically related to the enrichment ratio ($\rho = 0.95$), where $Z = \frac{(\text{observed } h_X^2 - \text{expected } h_X^2)}{\text{standard error}}$.

This enrichment Z-statistic was then used to obtain a corresponding P value, which was subsequently adjusted for the false discovery rate (FDR). For each chromosome, the proportion of genomic base pairs residing within the partition was calculated using assembly statistics for Genome Reference Consortium Human Build 37 (GRCh37) available at https://www.ncbi.nlm.nih.gov/assembly/GCF_000001405.13/.

Extended partitioned heritability analyses. To verify that the heritability estimate for a given chromosome was largely proportional to its genomic length (as previously reported³), we conducted extended GREML analyses that included a genetic variance component for each chromosome. Specifically, for the 56 regional SA phenotypes with significant enrichment of X-chromosome heritability, we extended the final GREML model to include a genetic variance component for each of the 23 chromosomes (22 autosomes and the X-chromosome). This yielded estimates of heritability per chromosome h_c^2 for each region. We then computed the mean and 95% CIs for each partition's h_c^2 estimate by averaging across regions, and plotted those values as a linear function of chromosome length. The line of best fit for these values showed a strong concordance to the theoretical expectation based on equal per-SNP heritability^{57,58}, and only the X-chromosome deviated substantially from the expected value.

Sensitivity analyses. We performed three additional analyses to interrogate the robustness of the final results for the 358 regional SA phenotypes: (1) release-stratified GREML (that is, two subsamples corresponding to the first and second releases of UKB neuroimaging data); (2) repeated GREML in 100 random split-halves of the sample; and (3) GREML with a more conservative MAF threshold (0.001 versus 0.0003). In the release-stratified GREML analyses, we re-estimated model parameters and computed the enrichment Z-statistics in each subsample. We then computed the cross-ROI correlation of those Z-statistics across releases. In the repeated GREML analyses, we re-estimated model parameters and computed the enrichment Z-statistics in 100 random split-halves of the sample, holding the ratio of females and males to be the same in both matching halves. For this analysis, we computed the cross-ROI correlation for each pair of split-halves, which generated a distribution of correlation values that further indexed the reliability of our results. Finally, in the GREML analyses employing a more conservative MAF threshold, we applied the same quality control procedures and conducted the same statistical analysis with one exception: we filtered out SNPs with a MAF less than 0.001 before constructing the GRMs. Here, the cross-ROI correlation of enrichment Z-statistics across MAF thresholds was computed.

To test whether the cortical parcellation scheme influenced the estimates of regional XIs on SA, we also repeated the final GREML analyses for SA using a 308-region cortical parcellation²⁵ that has been widely used in prior work. Also, a pre-calculated scheme based on rotations of this 308-region parcellation provides a nonparametric permutation test of the significance of spatial correlations between two regional maps while accounting for the shared spatial autocorrelation and the

arbitrary variations in power that would otherwise arise from changes in spatial resolution^{26,27}. Based on the coordinates of the HCP and 308 parcellations defined in the shared FreeSurfer cortical space, we projected the XI Z-statistics for SA in the HCP-parcellation to the 308-parcellation (by averaging the values in each of the 308 parcels) and calculated the cross-parcel Pearson's correlation between these XI Z-statistics for SA (that is, projected from the HCP) and those directly calculated in the 308 parcellation. The statistical significance of this observed correlation was determined by the nonparametric spin test described below.

Spin tests. To assess the specificity of the correspondence between pairs of cortical maps, we generated 10,000 rotations (that is, spins) of the cortical parcellation^{27,59}. A measure of observed spatial correspondence between two maps of interest could then be compared against the null distribution of measures generated from using the spun maps. Importantly, the spin approach allows any regional measure to be permuted while controlling for spatial contiguity and hemispheric symmetry. We first obtained the spherical surface coordinates for the centroid of each ROI within the 308 cortical regions on the fsaverage template in FreeSurfer. These were then rotated about the three principal axes at three randomly generated angles. Given the separate left- and right-hemisphere cortical projections, and to preserve symmetry, the same random angles were applied to both hemispheres with the caveat that the sign of the angles was flipped for the rotation around the y and z axes. Following each rotation, the coordinates of the rotated regions were matched to the coordinates of the initial regions using Euclidean distance, proceeding in descending order of average Euclidean distance between pairs of regions on the rotated and unrotated spheres (that is, starting with the rotated region that is furthest away, on average, from the unrotated regions).

Topographic annotation of brain regions with enriched X-linked heritability. We examined the spatial coupling between enriched XIs on cortical SA and topography of the Yeo–Krienen cortical parcellation, which classifies 17 functional intrinsic connectivity networks derived from resting-state functional MRI data²⁸. We assigned a label of 1 to 17 from the Yeo–Krienen parcellation to each parcel of the 308-parcellation by identifying the maximum overlap among the 17 networks with that parcel. A primary omnibus test first was used to examine whether the spatial distribution of XIs on SA was related to topography of the Yeo–Krienen-parcellation. To achieve this test, we recorded the observed F -test value of a regression model with XI Z-statistics for regional SA as the dependent variable, and the Yeo–Krienen assignments as the independent variable. We then compared this observed F value against a distribution of 10,000 null F values from repeating the above regression models using spun versions of XI Z-statistics for regional SA (see ‘Spin tests’ above). Given a detection of a significant omnibus association, follow-up post hoc spin tests were used to identify which specific components of the Yeo–Krienen-parcellation showed overlaps with enriched XIs on SA. Specifically, we used Fisher's exact tests to compute the observed odds ratio for overlap between each of the 17 Yeo–Krienen networks and regions of significant XI enrichment for SA. A nominal P value was derived for each network by comparing its observed odds ratio with 10,000 null odds ratios from spun versions of significant XI enrichment for SA.

We also compared the spatial pattern of enriched XIs on SA to functional anatomy of the human brain as described by Neurosynth (<https://neurosynth.org>), an online platform for meta-analysis of functional neuroimaging literature³⁹. Previously, a topic modeling technique was applied to the text of over 11,000 studies in the Neurosynth database to define a set of 50 topics capturing conceptually distinct aspects of human cognition⁶⁰. Each topic represents a cluster of weighted text terms with shared relevance for a common overarching cognitive construct and is tagged with a specific association test map, in which each voxel's association statistic (Z-score) represents the likelihood that that voxel is preferentially activated by the topic in question over all other topics. To exclude association test maps that lack meaningful results, we applied an empirical filter to these 50 maps and retained 30 significant maps with at least one cluster of greater than 100 contiguous voxels after correcting for FDR.

For each of these 30 Neurosynth association test maps, we assigned each parcel of 308 to 1 if there was an overlap between the significant regions in the association test map and that parcel, to 0 if not. Again, a primary omnibus test was used to determine whether the spatial distribution of XIs on SA was non-randomly related to the topography of regional cortical activation for the 30 Neurosynth topics. Specifically, for each Neurosynth topic term, we calculated the F -test value of a regression model with XI Z-statistics for regional SA as the dependent variable and the binary Neurosynth assignments for that term in the 308 parcellation as the independent variable. We then compared the average of these F values across all 30 Neurosynth topics, with the null distribution of this average F value from 10,000 spins of XI Z-statistics for regional SA. Given a detection of a significant omnibus association, follow-up post hoc spin tests were used to identify which specific Neurosynth topic maps showed an overlap with enriched XIs on SA. Specifically, we used Fisher's exact tests to compute the observed odds ratio for overlap between each Neurosynth topic map and regions of significant XI enrichment for SA. A nominal P value was derived for each Neurosynth topic by comparing its observed odds ratio with 10,000 null odds ratios from spun versions of significant XI enrichment for SA. Given the aim of annotating enriched XIs on SA, the omnibus

tests above excluded those regions with evidence of significant depletion of XIs on SA (Extended Data Fig. 8).

X-chromosome association analyses. We used PLINK (v.2.00) to conduct a series of SNP-based XWA tests for SA phenotypes with significantly enriched X-chromosome heritability. As previously noted, females were coded as diploid (0, 1 or 2) and males were analyzed as homozygous diploid (0 or 2) in accordance with the full dosage compensation model. The final analytic sample in the GREML analyses (that is, the unrelated imaging sample) was selected as the analytic sample for association analyses. Hard call genotypes were analyzed by fitting the linear model $y = X\beta_X + G\beta_G + \epsilon$ for each SNP, where y is the phenotype, X is the covariate matrix, G is the genotype matrix for the target SNP and ϵ is the error term. Paralleling the GREML analyses, the first 20 principal components of ancestry, sex, age, genotyping batch and scanning site were included as covariates. We then used an established EasyQC (v.9.2)⁶¹ pipeline to perform additional quality control on the GWAS summary statistics, as described in previous studies^{62,63}. Here, we filtered out rare and low-frequency SNPs ($MAF < 0.005$), SNPs that were not imputed well (imputation score < 0.60), SNPs that were unavailable or discordant with the reference panel (a combination of 1000 Genomes Phase 3 v.5 and UK10K data) or SNPs that had implausible values (for example, $P > 1$). There were 240,400 X-chromosome SNPs suitable for gene-based testing after applying these quality control filters. Finally, after subjecting the XWA summary statistics to quality control, we used MAGMA (v.1.08)⁶⁴ to conduct gene-based association analyses for 724 X-linked genes. Here, we used default MAGMA parameters and followed standard procedures for gene-based association analyses as implemented in FUMA⁶⁵.

Biological annotation of associated genes. The disease relevance of the genes identified in gene-based XWA analyses was investigated via Enrichr⁶⁶, which used Fisher's exact test to evaluate whether the XWA gene set was enriched in gene–disease ontologies indexed by DisGeNET⁶⁷. In Enrichr, the human genome is used as the ‘background’ set and P values were corrected for FDR. To provide an independent and more conservative test of enrichment, we used a hypergeometric test to evaluate whether the XWA gene set was enriched for a curated list of genes implicated in developmental disorders by the DDD project ('probable' or 'confirmed' developmental disorder genes)^{32,53}. Here, we identified brain-expressed genes (per the Human Protein Atlas³¹; <https://www.proteinatlas.org/humanproteome/brain>) as the background set to conduct a more conservative test of enrichment.

To further evaluate the developmental relevance of the identified genes, we characterized their expression trajectory in the PsychENCODE dataset³⁴. Specifically, we applied weighted gene correlation network analysis (using the WGCNA (v.1.69) package in R)^{34,68} to the PsychENCODE data to compute a weighted average expression profile (eigengene), treating the gene set as a module. We then plotted expression as a function of sample age, using a locally estimated scatter plot smoothing line-of-best-fit to characterize the temporal pattern of gene set expression in cortical tissue. Inspection of this line (and the accompanying 95% CI) indicated that these genes were differentially expressed across development.

Reporting Summary. Further information on research design is available in the Nature Research Reporting Summary linked to this article.

Data availability

No data were collected as part of this study. All genetic and phenotypic data (including neuroimaging data) are available from the UKB via their standard data access procedure, as described at <https://www.ukbiobank.ac.uk/register-apply>. The Neurosynth data for topic-based meta-analyses are available at <https://neurosynth.org/analyses/topics/>. The PsychENCODE data for developmental expression analyses are available at <http://development.psychencode.org>. XWA summary statistics are available at <https://osf.io/cqxdj/>.

Code availability

No custom software was used in this study. All relevant software and code are described in the text and can be found at the URLs or references cited.

References

44. Sudlow, C. et al. UK Biobank: an open access resource for identifying the causes of a wide range of complex diseases of middle and old age. *PLoS Med.* **12**, e1001779 (2015).
45. Alfaro-Almagro, F. et al. Image processing and quality control for the first 10,000 brain imaging datasets from UK Biobank. *NeuroImage* **166**, 400–424 (2018).
46. Glasser, M. F. et al. The minimal preprocessing pipelines for the Human Connectome Project. *NeuroImage* **80**, 105–124 (2013).
47. Fischl, B. FreeSurfer. *NeuroImage* **62**, 774–781 (2012).
48. Ségonne, F. et al. A hybrid approach to the skull stripping problem in MRI. *NeuroImage* **22**, 1060–1075 (2004).
49. Dale, A. M., Fischl, B. & Sereno, M. I. Cortical surface-based analysis. I. Segmentation and surface reconstruction. *NeuroImage* **9**, 179–194 (1999).
50. Fischl, B., Sereno, M. I. & Dale, A. M. Cortical surface-based analysis. II. Inflation, flattening, and a surface-based coordinate system. *NeuroImage* **9**, 195–207 (1999).
51. Desikan, R. S. et al. An automated labeling system for subdividing the human cerebral cortex on MRI scans into gyral based regions of interest. *NeuroImage* **31**, 968–980 (2006).
52. Bycroft, C. et al. The UK Biobank resource with deep phenotyping and genomic data. *Nature* **562**, 203–209 (2018).
53. O'Connell, J. et al. Haplotype estimation for biobank-scale data sets. *Nat. Genet.* **48**, 817–820 (2016).
54. Chang, C. C. et al. Second-generation PLINK: rising to the challenge of larger and richer datasets. *Gigascience* **4**, 7 (2015).
55. Burnham, K. P. & Anderson, D. R. *Model Selection and Multimodel Inference: A Practical Information-Theoretic Approach*. (Springer Science & Business Media, 2002).
56. Finucane, H. K. et al. Heritability enrichment of specifically expressed genes identifies disease-relevant tissues and cell types. *Nat. Genet.* **50**, 621–629 (2018).
57. Speed, D., Hemani, G., Johnson, M. R. & Balding, D. J. Improved heritability estimation from genome-wide SNPs. *Am. J. Hum. Genet.* **91**, 1011–1021 (2012).
58. Yang, J. et al. Common SNPs explain a large proportion of the heritability for human height. *Nat. Genet.* **42**, 565–569 (2010).
59. Seidlitz, J. et al. Morphometric similarity networks detect microscale cortical organization and predict inter-individual cognitive variation. *Neuron* **97**, 231–247.e7 (2018).
60. Poldrack, R. A. et al. Discovering relations between mind, brain, and mental disorders using topic mapping. *PLoS Comput. Biol.* **8**, e1002707 (2012).
61. Winkler, T. W. et al. Quality control and conduct of genome-wide association meta-analyses. *Nat. Protoc.* **9**, 1192–1212 (2014).
62. Mallard, T. T. et al. Multivariate GWAS of psychiatric disorders and their cardinal symptoms reveal two dimensions of cross-cutting genetic liabilities. Preprint at [bioRxiv https://doi.org/10.1101/603134](https://doi.org/10.1101/603134) (2020).
63. Mallard, T. T. et al. Item-level genome-wide association study of the Alcohol Use Disorders Identification Test in three population-based cohorts. *Am. J. Psychiatry* <https://doi.org/10.1176/appi.ajp.2020.20091390> (2021).
64. de Leeuw, C. A., Mooij, J. M., Heskes, T. & Posthuma, D. MAGMA: generalized gene-set analysis of GWAS data. *PLoS Comput. Biol.* **11**, e1004219 (2015).
65. Watanabe, K., Taskesen, E., van Bochoven, A. & Posthuma, D. Functional mapping and annotation of genetic associations with FUMA. *Nat. Commun.* **8**, 1826 (2017).
66. Kuleshov, M. V. et al. Enrichr: a comprehensive gene set enrichment analysis web server 2016 update. *Nucleic Acids Res.* **44**, W90–W97 (2016).
67. Pifero, J. et al. The DisGeNET knowledge platform for disease genomics: 2019 update. *Nucleic Acids Res.* **48**, D845–D855 (2020).
68. Langfelder, P. & Horvath, S. WGCNA: an R package for weighted correlation network analysis. *BMC Bioinformatics* **9**, 559 (2008).

Acknowledgements

This research was supported by the Intramural Research Program of the National Institute of Mental Health (NIH annual report number ZIA MH002949-04), and conducted using the UKB resource under application number 22875. We thank the UKB participants for making this study possible.

Author contributions

T.T.M. and A.R. conceived and designed the study. A.R. oversaw the study. T.T.M. was the lead analyst responsible for conducting all genetically informative analyses. S.L. conducted the topographic annotation analyses and spin tests. J.S. assisted with the expression analyses in the PsychENCODE dataset. T.T.M. and S.L. prepared the figures and tables. T.T.M. prepared the genetic data, while J.S., Z.M., D.M. and A.T. prepared the neuroimaging data. T.T.M. and A.R. led the writing of the manuscript, and all authors provided valuable feedback and advice during its preparation.

Competing interests

The authors declare no competing interests.

Additional information

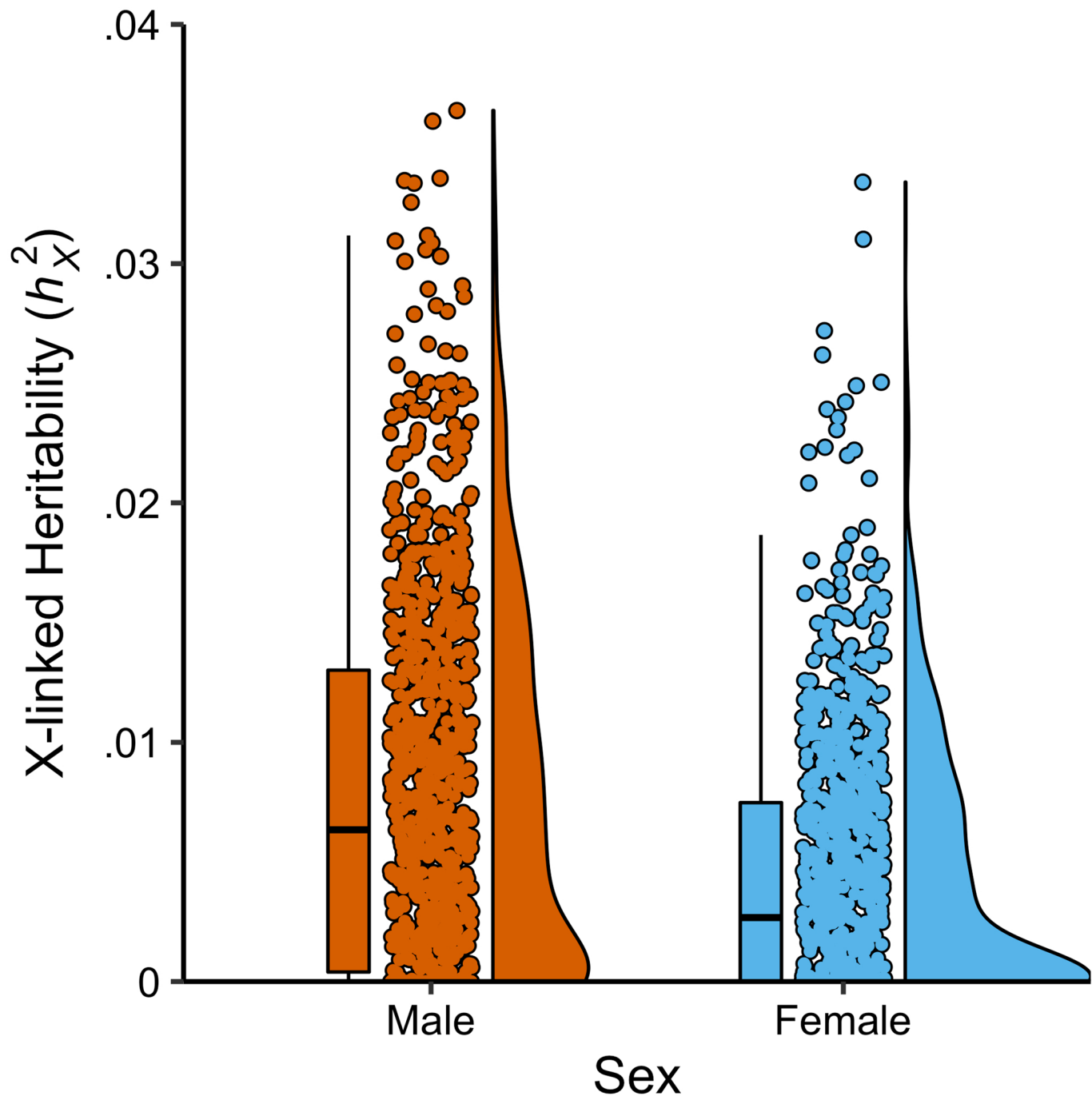
Extended data is available for this paper at <https://doi.org/10.1038/s41593-021-00890-w>.

Supplementary information The online version contains supplementary material available at <https://doi.org/10.1038/s41593-021-00890-w>.

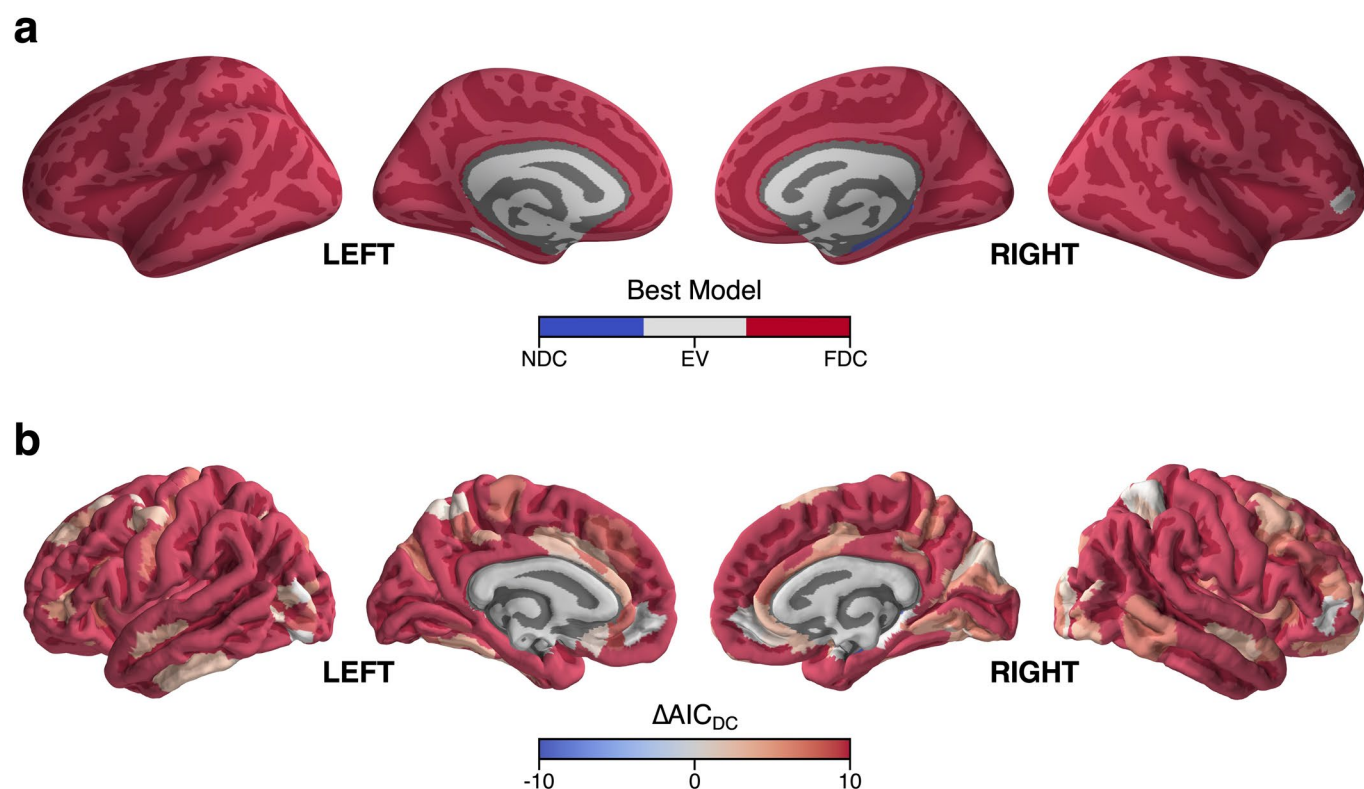
Correspondence and requests for materials should be addressed to A.R.

Peer review information *Nature Neuroscience* thanks Jason Stein and the other, anonymous, reviewer(s) for their contribution to the peer review of this work.

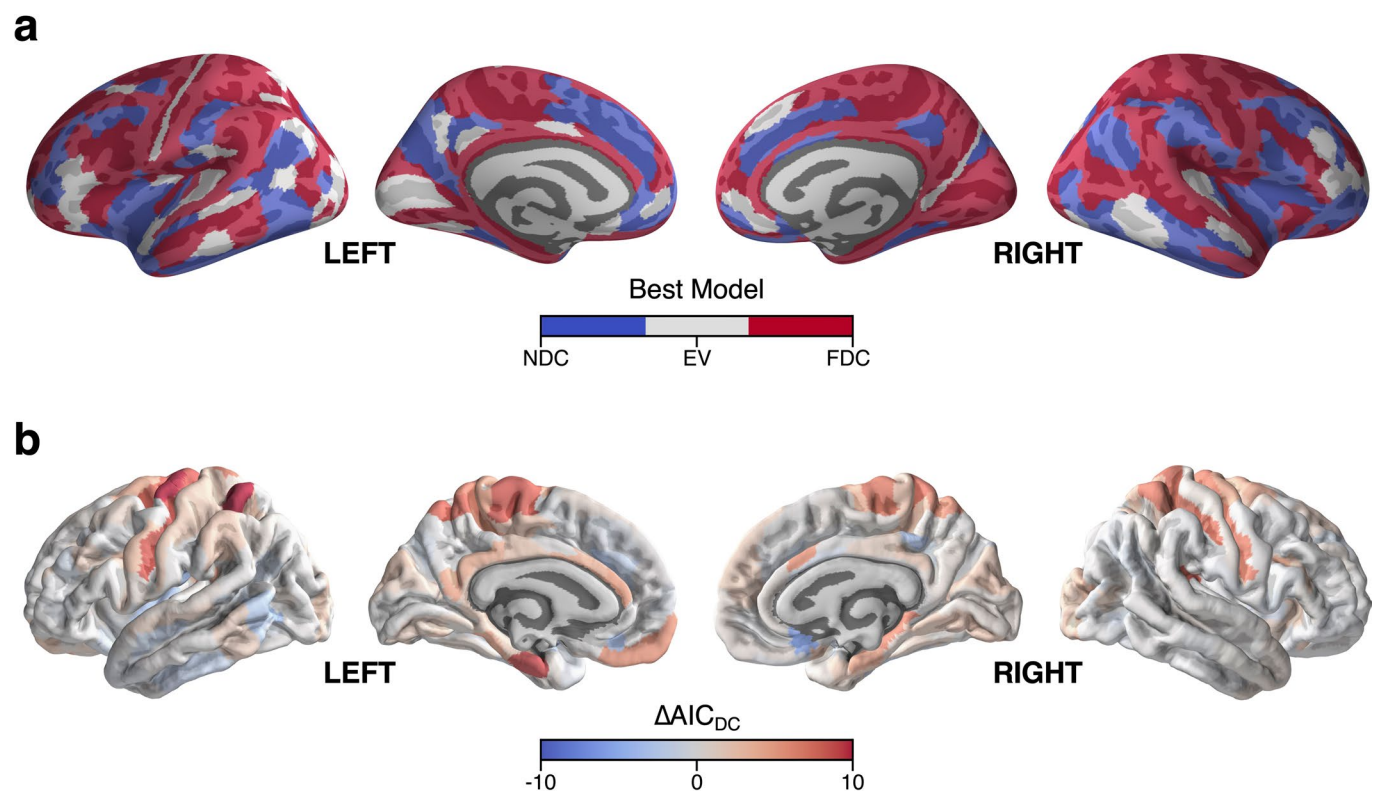
Reprints and permissions information is available at www.nature.com/reprints.



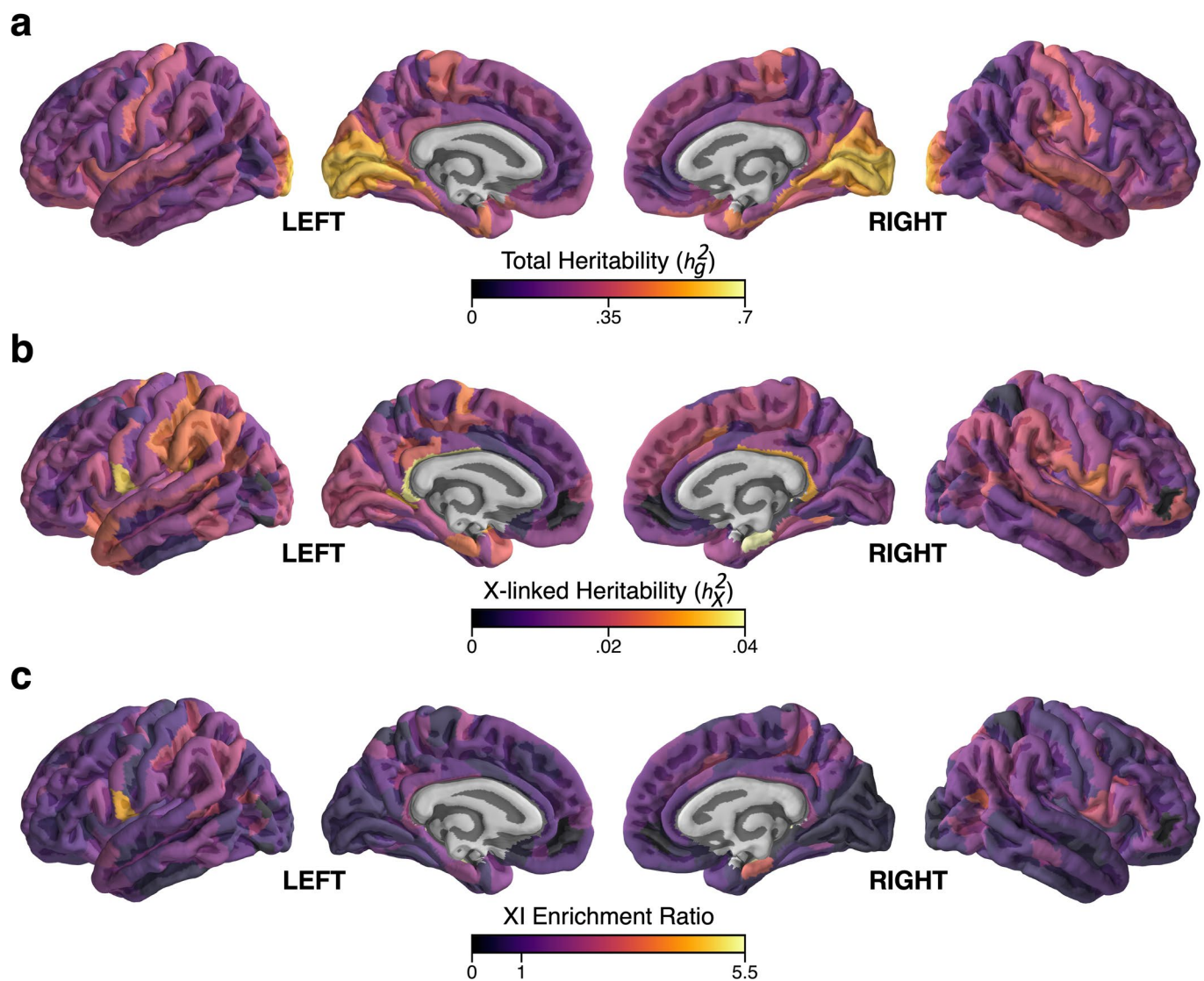
Extended Data Fig. 1 | Distributions of X-linked heritability in males and females for regional measures of brain anatomy. Raincloud-style plot that considers all regional measures of brain anatomy where the full dosage compensation model was the best fitting model ($n=1,840$ sex-stratified heritability estimates). X-linked heritability for males and females was independently estimated within each sex in a model-naïve manner (Methods). The median X-linked heritability in males is 2.37 times larger (bootstrapped 95% CI = 1.70–3.25) than the median X-linked heritability in females (two-sided Wilcoxon $P=1.18\text{e-}23$). Summary statistics for males: minimum = 1e-6, Q1 = 3.98e-4, median = 6.34e-3, Q3 = 1.3e-2, maximum = 3.64e-2. Summary statistics for females: minimum = 1e-6, Q1 = 1e-6, median = 2.67e-3, Q3 = 7.48e-3, maximum = 3.34e-2.



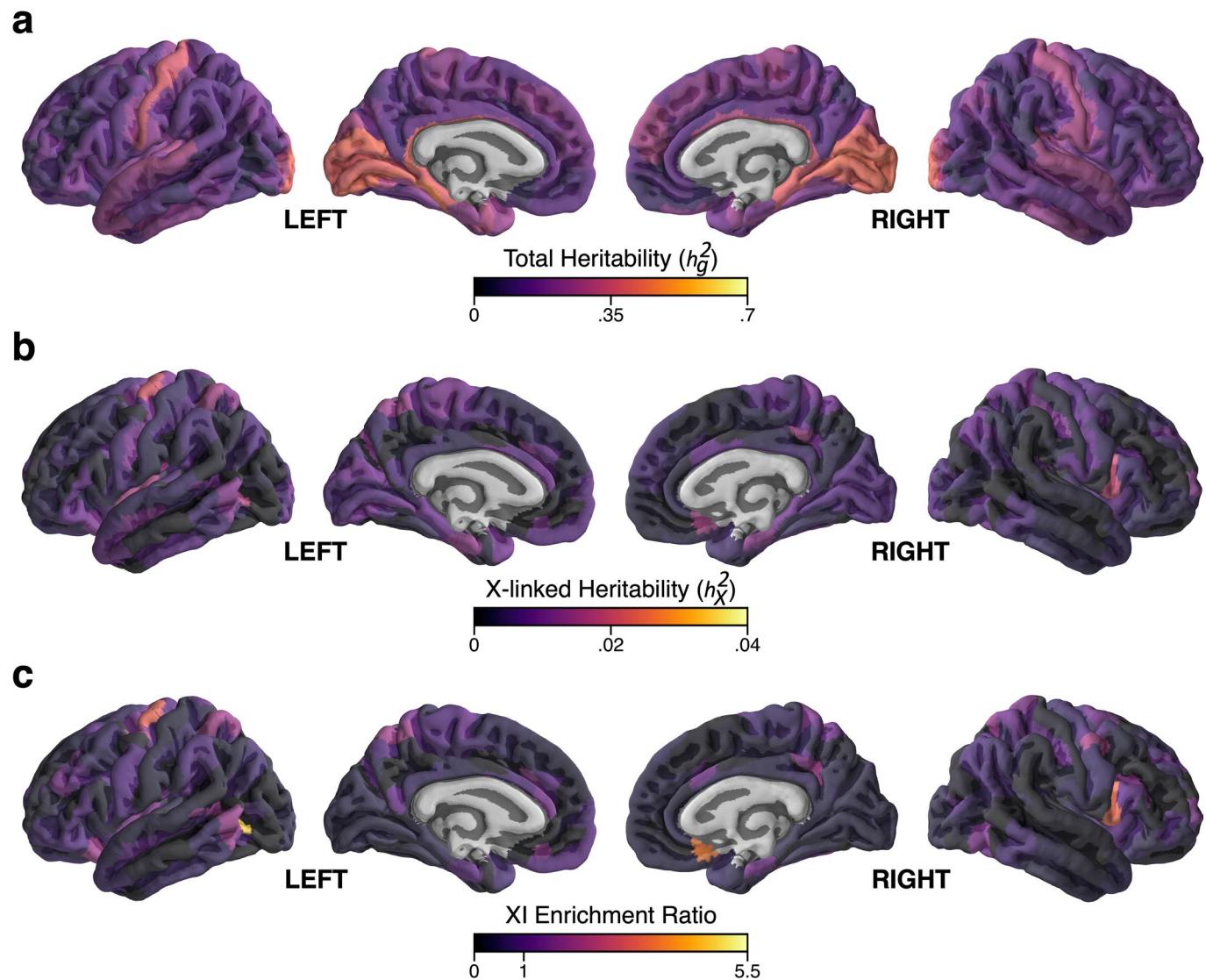
Extended Data Fig. 2 | Regional patterning of X-chromosome dosage compensation for cortical volume (CV). **a**, Categorical map showing the best-fitting X-chromosome dosage compensation model for each cortical region. NDC = no dosage compensation, EV = equal variance, FDC = full dosage compensation. **b**, Continuous map showing regional variation in the strength of statistical evidence for X-chromosome dosage compensation on CV, as indexed by $\Delta\text{AIC}_{\text{DC}}$ (Methods). $\Delta\text{AIC}_{\text{DC}}$ equals zero when the EV model fits best, and departures from zero reflect quantitative evidence for either NDC or FDC. Values ≤ -10 are indicative of strong evidence for NDC while values $\geq +10$ are indicative of strong evidence for FDC. Any values less than -10 or greater than 10 were set to -10 and 10 , respectively, for illustration.



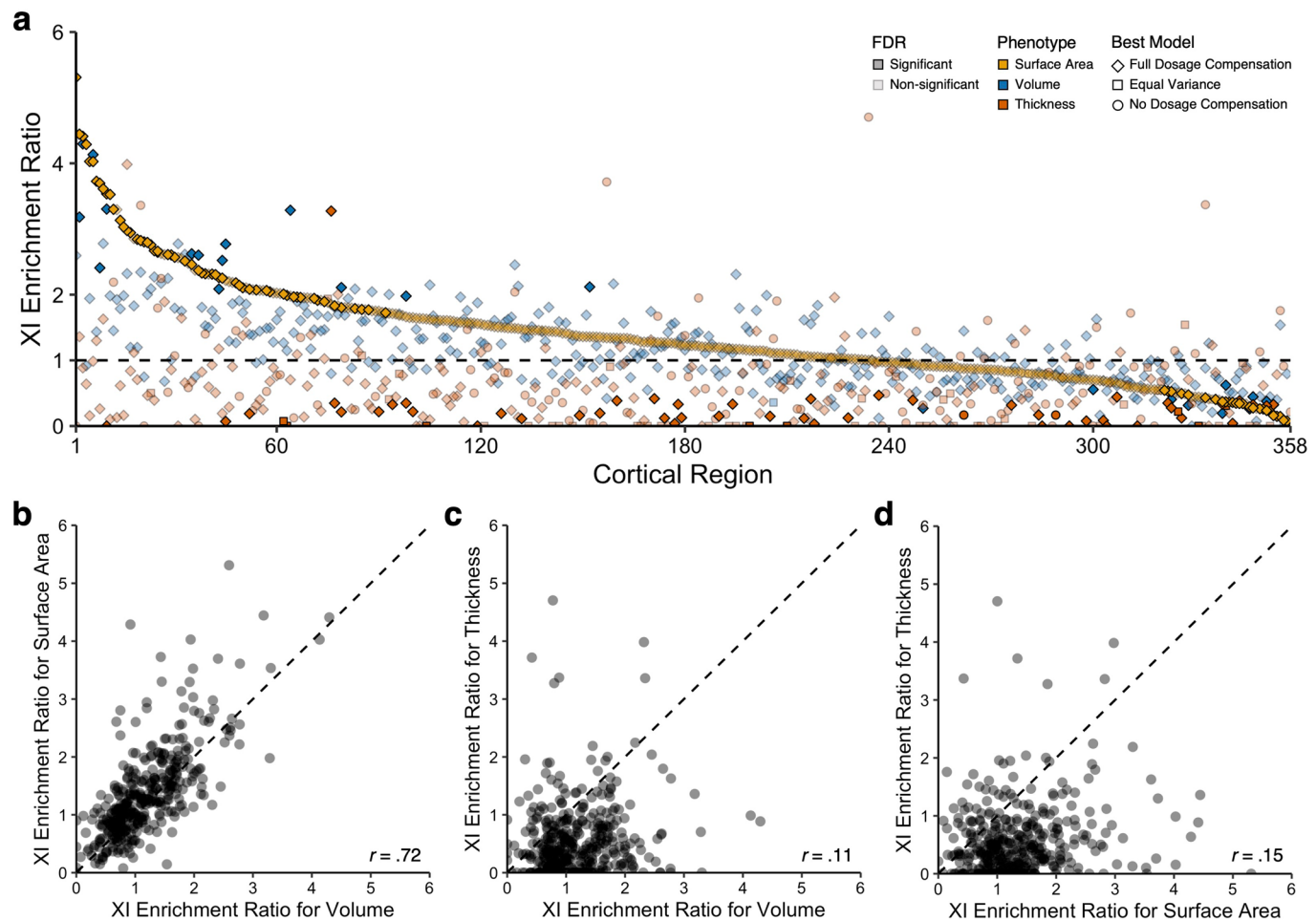
Extended Data Fig. 3 | Regional patterning of X-chromosome dosage compensation for cortical thickness (CT). **a**, Categorical map showing the best-fitting X-chromosome dosage compensation model for each cortical region. NDC = no dosage compensation, EV = equal variance, FDC = full dosage compensation. **b**, Continuous map showing regional variation in the strength of statistical evidence for X-chromosome dosage compensation on CT, as indexed by $\Delta\text{AIC}_{\text{DC}}$ (Methods). $\Delta\text{AIC}_{\text{DC}}$ equals zero when the EV model fits best, and departures from zero reflect quantitative evidence for either NDC or FDC. Values ≤ -10 are indicative of strong evidence for NDC while values $\geq +10$ are indicative of strong evidence for FDC. Any values less than -10 or greater than 10 were set to -10 and 10 , respectively, for illustration.



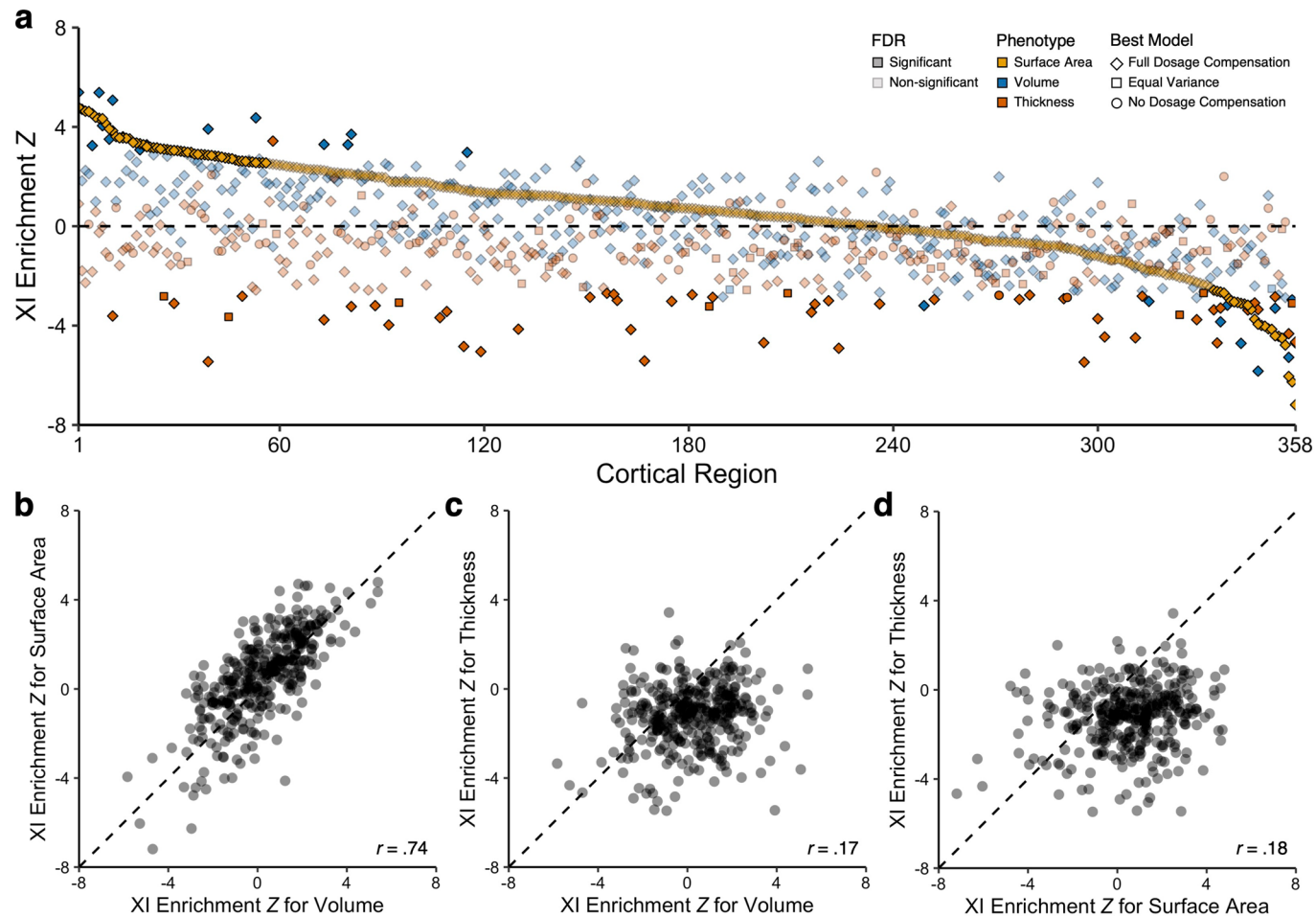
Extended Data Fig. 4 | Regional patterning of X-chromosome influences (XIs) on cortical volume (CV). **a**, Continuous map of total SNP heritability (h_g^2) for regional CV. **b**, Continuous map of X-linked heritability (h_x^2) for regional CV. **c**, Continuous map of regional ratio between the observed proportion of total heritability assigned to the X-chromosome, and the expected proportion from X-chromosome size (XI ratio). Values greater than one reflect enriched XIs and values less than one reflect depleted XIs (Methods).



Extended Data Fig. 5 | Regional patterning of X-chromosome influences (XIs) on cortical thickness (CT). **a**, Continuous map of total SNP heritability (h_g^2) for regional CT. **b**, Continuous map of X-linked heritability (h_x^2) for regional CT. **c**, Continuous map of regional ratio between the observed proportion of total heritability assigned to the X-chromosome, and the expected proportion from X-chromosome size (XI ratio). Values greater than one reflect enriched XIIs and values less than one reflect depleted XIIs (Methods).

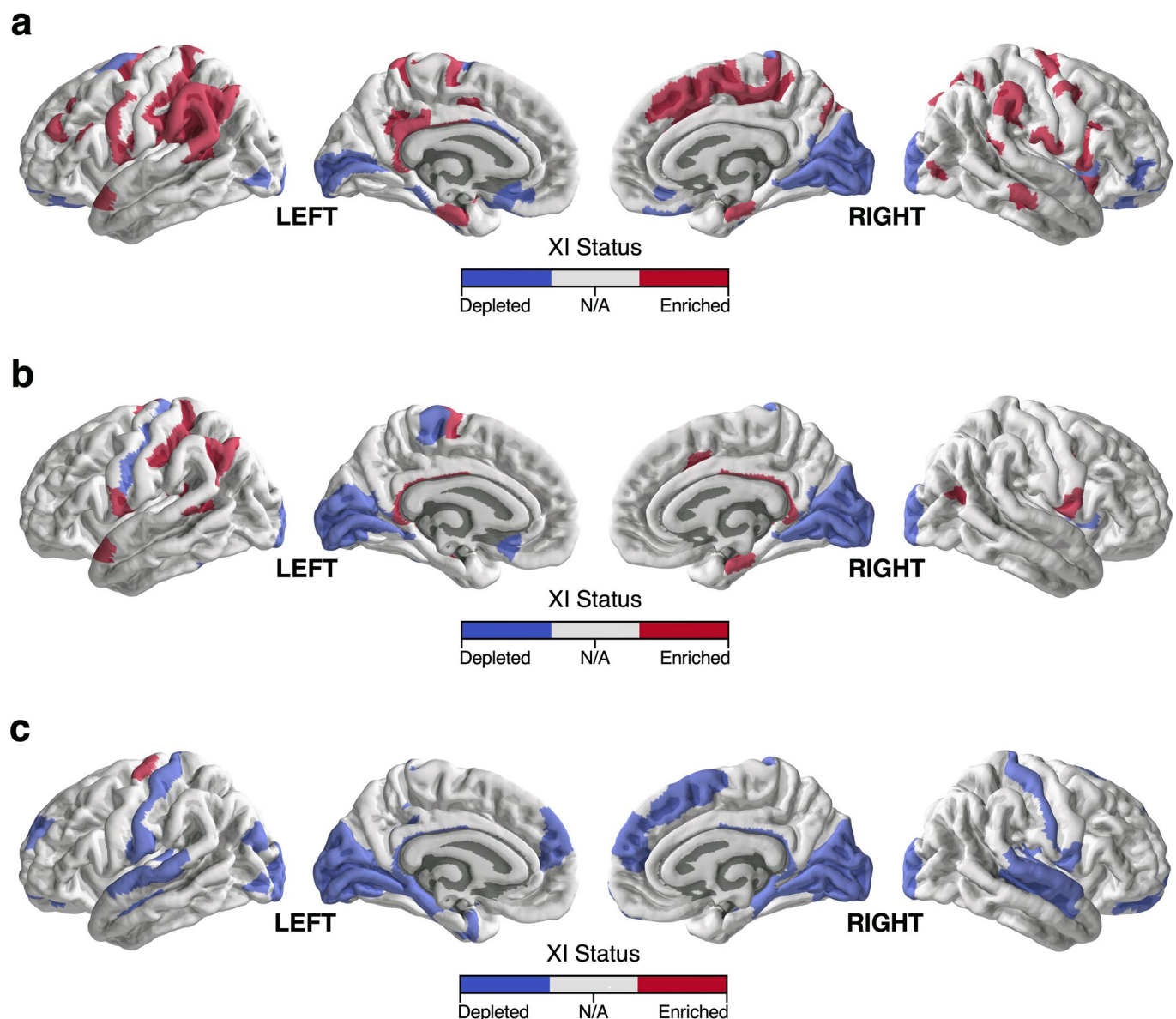


Extended Data Fig. 6 | Comparison of the enrichment ratio for X-chromosome influences (XIs) on three morphological features of the cortex. **a**, Ranked scatter plot of the regional XI enrichment ratio for cortical surface area, volume, and thickness, where the 358 cortical regions are ranked by their XI enrichment ratio for surface area. **b,c,d**, Scatter plots of the regional XI enrichment ratio for **(b)** surface area and volume, **(c)** thickness and volume, and **(d)** thickness and surface area.

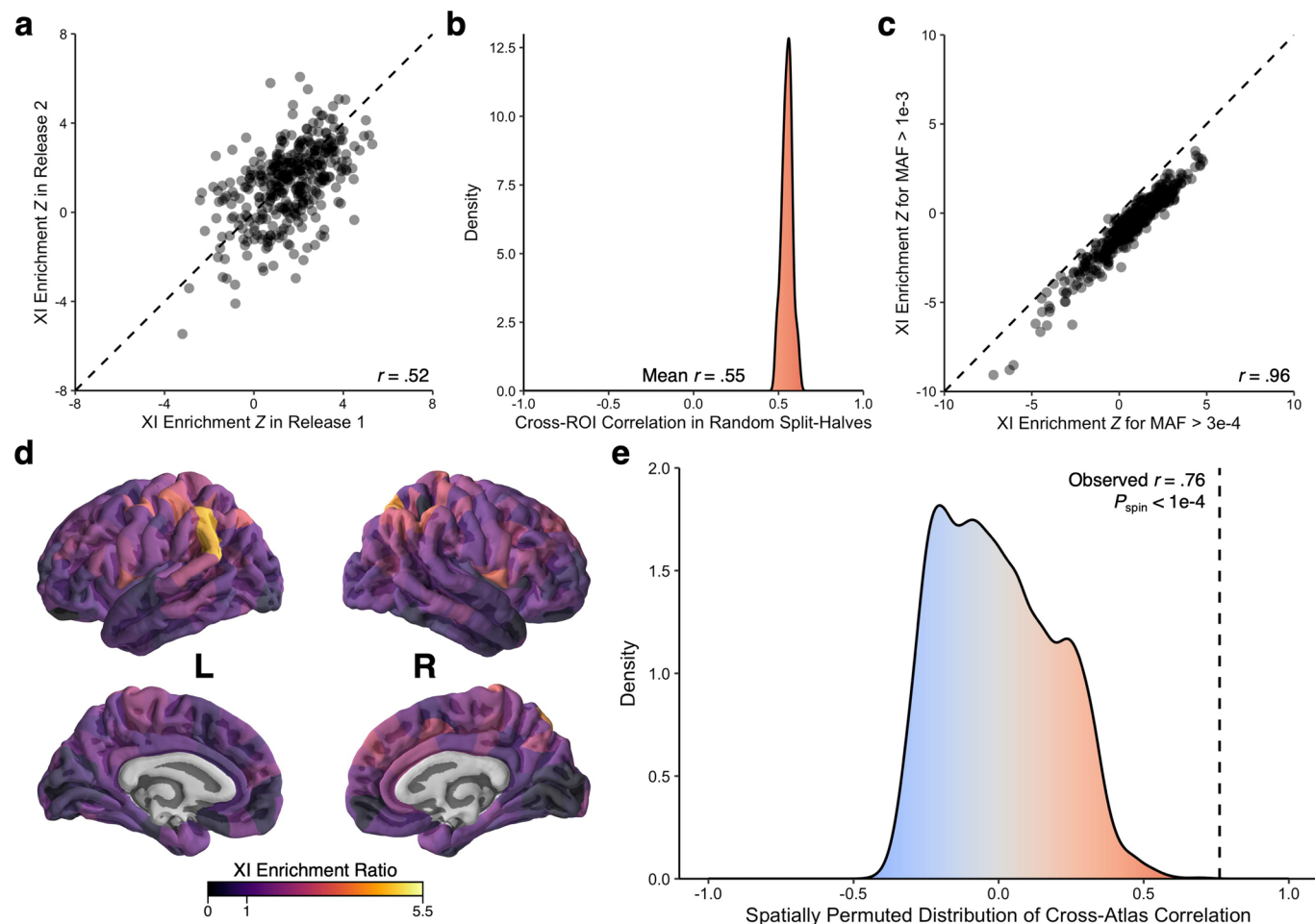


Extended Data Fig. 7 | Comparison of the enrichment Z statistic for X-chromosome influences (XIs) on three morphological features of the cortex.

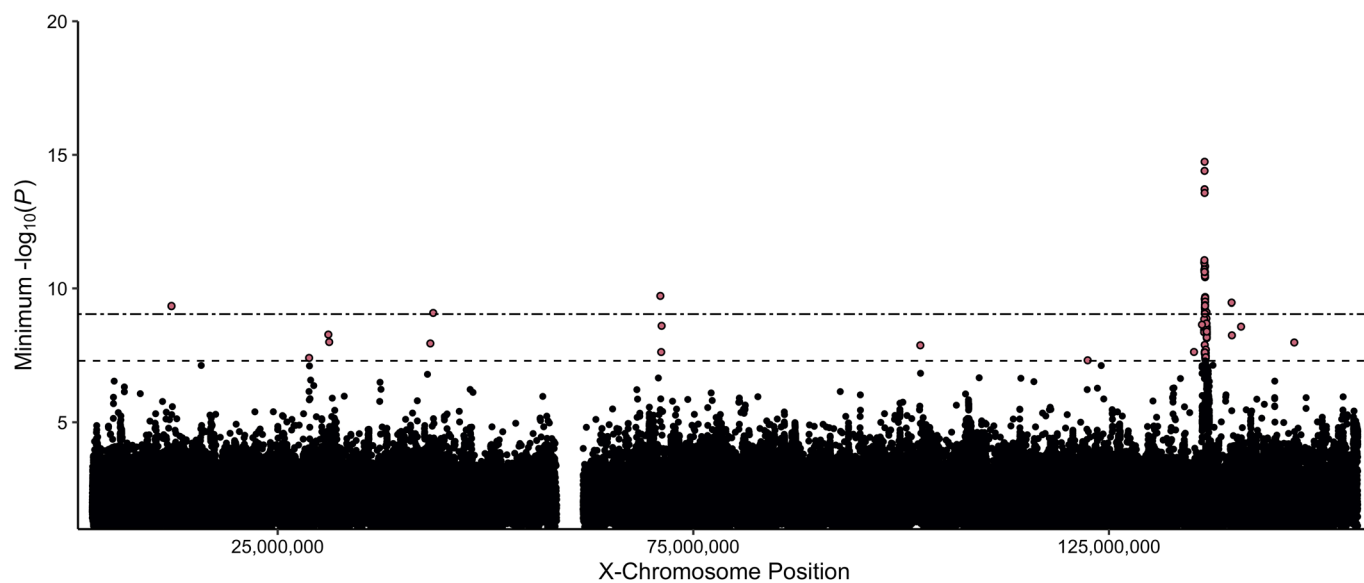
a, Ranked scatter plot of the regional XI enrichment Z-statistic for cortical surface area, volume, and thickness, where the 358 cortical regions are ranked by their XI enrichment Z-statistic for surface area. **b,c,d**, Scatter plots of the regional XI enrichment Z-statistic for **(b)** surface area and volume, **(c)** thickness and volume, and **(d)** thickness and surface area.



Extended Data Fig. 8 | Statistically-significant depletion and enrichment of X-chromosome influences (XIs) on three morphological features of the cortex. **a,b,c**, Categorical maps showing the regions of statistically significant depletion or enrichment of XIs (after correction for multiple comparisons) on (a) cortical surface area, (b) cortical volume, and (c) cortical thickness.



Extended Data Fig. 9 | Sensitivity analyses for observed X-chromosome influences (XIs) on cortical surface area (SA). **a**, Cross-region of interest (ROI) correlation in the XI Z-statistic for SA between first and second releases of UKB neuroimaging data. **b**, Distribution of cross-ROI correlations in the XI Z-statistic for SA for 100 split-halves of the UKB dataset. **c**, Cross-ROI correlation in the XI Z-statistic for SA between UKB analyses differing in minor allele frequency (MAF) threshold. **d**, Continuous map of XI enrichment ratio for SA as computed in the 308-parcellation. **e**, Observed cross-ROI correlation (dashed line) in the 308-parcellation between XI Z-statistics computed in the 308-parcellation vs. those projected into the 308-parcellation from values computed in the primary HCP atlas. Density plot shows a null distribution of these correlations from 10,000 rotational permutations ‘spins’ of the 308 map. The observed correlation (two-sided Pearson’s $r = .76$) is significantly elevated relative to this null distribution ($P_{\text{spin}} < 1e-4$) (Methods).

**Extended Data Fig. 10 | X-linked SNPs associated with regional surface area phenotypes with enriched X-chromosome influences (XIs).**

An X-chromosome-wide Manhattan plot of the minimum P -value for each SNP across all tested phenotypes. The x-axis refers to the chromosomal position, the y-axis refers to the significance of the SNP-based association test as a $-\log_{10} P$ -value, the horizontal dashed line denotes genome-wide significance ($P=5\text{e-}8$), and the horizontal two-dashed line denotes a more conservative significance threshold accounting for all tested phenotypes ($P=8.93\text{e-}10$).

Corresponding author(s): Dr. Armin Raznahan

Last updated by author(s): Jun 10, 2021

Reporting Summary

Nature Research wishes to improve the reproducibility of the work that we publish. This form provides structure for consistency and transparency in reporting. For further information on Nature Research policies, see our [Editorial Policies](#) and the [Editorial Policy Checklist](#).

Statistics

For all statistical analyses, confirm that the following items are present in the figure legend, table legend, main text, or Methods section.

n/a Confirmed

- The exact sample size (n) for each experimental group/condition, given as a discrete number and unit of measurement
- A statement on whether measurements were taken from distinct samples or whether the same sample was measured repeatedly
- The statistical test(s) used AND whether they are one- or two-sided
Only common tests should be described solely by name; describe more complex techniques in the Methods section.
- A description of all covariates tested
- A description of any assumptions or corrections, such as tests of normality and adjustment for multiple comparisons
- A full description of the statistical parameters including central tendency (e.g. means) or other basic estimates (e.g. regression coefficient) AND variation (e.g. standard deviation) or associated estimates of uncertainty (e.g. confidence intervals)
- For null hypothesis testing, the test statistic (e.g. F , t , r) with confidence intervals, effect sizes, degrees of freedom and P value noted
Give P values as exact values whenever suitable.
- For Bayesian analysis, information on the choice of priors and Markov chain Monte Carlo settings
- For hierarchical and complex designs, identification of the appropriate level for tests and full reporting of outcomes
- Estimates of effect sizes (e.g. Cohen's d , Pearson's r), indicating how they were calculated

Our web collection on [statistics for biologists](#) contains articles on many of the points above.

Software and code

Policy information about [availability of computer code](#)

Data collection As no new data were collected in this study, there is no custom software or code to report here.

Data analysis No custom software was used in this study. All relevant software and code are described in the text and can be found at the URLs or references cited. A list of key software used in this study follows: Human Connectome Project pipeline v3, FreeSurfer v5.3.0, PLINK v1.90, PLINK v2.00, GCTA v1.92.1beta6, R v3.6.2, R v4.0.3, EasyQC v9.2, MAGMA v1.08, WGCNA v1.69. Note that some software described in the Methods (e.g., SHAPEIT3, IMPUTE4) were only used by the original UK Biobank investigators, and are only described in the current manuscript for clarity.

For manuscripts utilizing custom algorithms or software that are central to the research but not yet described in published literature, software must be made available to editors and reviewers. We strongly encourage code deposition in a community repository (e.g. GitHub). See the Nature Research [guidelines for submitting code & software](#) for further information.

Data

Policy information about [availability of data](#)

All manuscripts must include a [data availability statement](#). This statement should provide the following information, where applicable:

- Accession codes, unique identifiers, or web links for publicly available datasets
- A list of figures that have associated raw data
- A description of any restrictions on data availability

No data was collected as part of this study. All genetic and phenotypic data (including neuroimaging data) are available from the UK Biobank via their standard data access procedure, as described at <https://www.ukbiobank.ac.uk/register-apply>. The Neurosynth data for topic-based meta-analyses is available at <https://neurosynth.org/analyses/topics/>. The PsychENCODE data for developmental expression analyses is available at <http://development.psychencode.org>. XWAS summary statistics are available at <https://osf.io/cqxdj/>.

Field-specific reporting

Please select the one below that is the best fit for your research. If you are not sure, read the appropriate sections before making your selection.

- Life sciences Behavioural & social sciences Ecological, evolutionary & environmental sciences

For a reference copy of the document with all sections, see nature.com/documents/nr-reporting-summary-flat.pdf

Behavioural & social sciences study design

All studies must disclose on these points even when the disclosure is negative.

Study description

The present study is a quantitative study of the UK Biobank. It is a genetically-informative study that quantifies the influence of the X chromosome on individual differences in neuroanatomy, as measured via structural magnetic resonance imaging (MRI).

Research sample

The UK Biobank (UKB) is a large-scale biomedical study designed to investigate the influence of genetic and environmental variables on human health and wellbeing. All participants provided informed consent, were genotyped, and completed a myriad of questionnaires related to complex traits. A subset of participants also took part in a MRI protocol, where they attended a scanning appointment at one of three sites. The final sample size for the present study was 32,256 (52.97% female, mean age = 64.31). Data and materials are available via UK Biobank (<https://www.ukbiobank.ac.uk>).

Sampling strategy

The UK Biobank is a large population-based biobank that is largely representative of the UK population. Details on the sampling strategy can be found at <https://www.ukbiobank.ac.uk>, as well as in studies previously published by the original UK Biobank investigators. We selected the UK Biobank as our analytic sample, as it is (1) the largest sample with the types of data required for these analyses, and (2) well-powered for GREML-based heritability analyses.

Data collection

No new data was collected for this study. Only existing data was analyzed. Details on the data collection strategy of the UK Biobank can be found at <https://www.ukbiobank.ac.uk>, as well as in studies previously published by the original UK Biobank investigators.

Timing

No new data was collected for this study. Only existing data was analyzed. Details on the timing of data collection of the UK Biobank can be found at <https://www.ukbiobank.ac.uk>, as well as in studies previously published by the original UK Biobank investigators. The official website of UK Biobank states that data collection began in 2006 and some related activities continue to present day.

Data exclusions

We made use of all available data that passed quality control thresholds. Data was only excluded if the data were considered low quality per standard conventions in the field. All data exclusion criteria are thoroughly described in the Methods section of the manuscript.

Non-participation

As we did not collect the data, we are not privy to information regarding non-participation.

Randomization

N/A. Covariates were included in all statistical models.

Reporting for specific materials, systems and methods

We require information from authors about some types of materials, experimental systems and methods used in many studies. Here, indicate whether each material, system or method listed is relevant to your study. If you are not sure if a list item applies to your research, read the appropriate section before selecting a response.

Materials & experimental systems

- | | |
|-------------------------------------|---|
| n/a | Involved in the study |
| <input checked="" type="checkbox"/> | <input type="checkbox"/> Antibodies |
| <input checked="" type="checkbox"/> | <input type="checkbox"/> Eukaryotic cell lines |
| <input checked="" type="checkbox"/> | <input type="checkbox"/> Palaeontology and archaeology |
| <input checked="" type="checkbox"/> | <input type="checkbox"/> Animals and other organisms |
| <input type="checkbox"/> | <input checked="" type="checkbox"/> Human research participants |
| <input checked="" type="checkbox"/> | <input type="checkbox"/> Clinical data |
| <input checked="" type="checkbox"/> | <input type="checkbox"/> Dual use research of concern |

Methods

- | | |
|-------------------------------------|--|
| n/a | Involved in the study |
| <input checked="" type="checkbox"/> | <input type="checkbox"/> ChIP-seq |
| <input checked="" type="checkbox"/> | <input type="checkbox"/> Flow cytometry |
| <input type="checkbox"/> | <input checked="" type="checkbox"/> MRI-based neuroimaging |

Human research participants

Policy information about [studies involving human research participants](#)

Population characteristics

See above.

Recruitment

See above.

Ethics oversight

This research was supported by the Intramural Research Program of the National Institute of Mental Health (NIH Annual Report Number, ZIA MH002794-13), and conducted using the UK Biobank Resource under Application Number 22875. Ethical approval for the UK Biobank study was obtained by the original investigators.

Note that full information on the approval of the study protocol must also be provided in the manuscript.

Magnetic resonance imaging

Experimental design

Design type

No functional MRI data was analyzed in the present study.

Design specifications

No functional MRI data was analyzed in the present study.

Behavioral performance measures

No functional MRI data was analyzed in the present study.

Acquisition

Imaging type(s)

T1-weighted and T2 FLAIR structural scans were acquired on a Siemens Skyra 3T scanner.

Field strength

3 Tesla.

Sequence & imaging parameters

For T1-weighted imaging, a 3D MPRAGE sequence was used with 1 mm sagittal slices, 1 x 1 mm in-plane resolution, in-plane acceleration iPAT=2, and prescan-normalization. For T2 FLAIR imaging, a 3D SPACE sequence was used with 1.05 mm sagittal slices, 1 x 1 mm in-plane resolution, in-plane acceleration iPAT=2, partial Fourier = 7/8, fat saturation, elliptical k-space scanning, and prescan-normalization.

Area of acquisition

Whole brain.

Diffusion MRI

Used

Not used

Preprocessing

Preprocessing software

We used the PreFreeSurfer and FreeSurfer pipelines from the Human Connectome Project pipeline v3 (<https://github.com/Washington-University/HCPpipelines>) for the data pre-processing of the T1-weighted and T2 FLAIR MRI scans.

Normalization

Nonlinear registration of MRI images.

Normalization template

fsaverage surface template.

Noise and artifact removal

N/A. No functional MRI data was analyzed in the present study.

Volume censoring

N/A. No functional MRI data was analyzed in the present study.

Statistical modeling & inference

Model type and settings

We performed a series of genome-based restricted maximum likelihood (GREML) analyses in GCTA (Genome Wide Complex Trait Analysis) to (i) evaluate evidence for dosage compensation, (ii) partition heritability across chromosomes, and (iii) test for enriched X-linked heritability for 1,091 morphological phenotypes, corresponding to cortical surface area, thickness, and volume estimates for 358 standard regions of interest (ROIs), 14 subcortical volume ROIs, and 3 global phenotypes (total volume, total surface area, mean thickness).

Effect(s) tested

Dosage compensation (of X-chromosome), partitioned heritability across all chromosomes, and X-chromosome heritability enrichment of the neuroimaging phenotypes.

Specify type of analysis:

Whole brain

ROI-based

Both

Our primary analyses were focused on the following neuroanatomical phenotypes:

- i. 358 cortical ROIs (N=180 for each hemisphere) for each phenotype (cortical surface area, thickness, and volume) from the HCP parcellation,
- ii. 14 non-cortical ROIs for volume, and
- iii. 3 global phenotypes (total volume, total surface area, mean thickness).

We also used an alternative gyral-based (i.e., anatomically-driven) "308-parcellation" was used for a sensitivity analysis (see Methods).

Statistic type for inference
(See [Eklund et al. 2016](#))

Correlation (Pearson's r) was used to test for similarity between cortical brain maps. Wilcoxon rank test was used for testing median differences in sex-stratified analyses. Heritability estimates and enrichment ratios were used to quantify genetic effects.

Correction

FDR correction & rotation-based permutation testing of the cortical brain maps (https://github.com/frantisekvasa/rotate_parcellation).

Models & analysis

n/a	Involved in the study
<input checked="" type="checkbox"/>	Functional and/or effective connectivity
<input checked="" type="checkbox"/>	Graph analysis
<input checked="" type="checkbox"/>	Multivariate modeling or predictive analysis